Hybrid Galerkin numerical modelling of elastodynamics and compressible Navier–Stokes couplings: applications to seismo-gravito acoustic waves

Quentin Brissaud, Roland Martin, Raphaël F. Garcia, Dimitri Komatitsch

Geophysical Journal International

Geophys. J. Int. (2017) **210,** 1047–1069
Advance Access publication 2017 May 4
GJI Seismology

doi: 10.1093/gji/ggx185

Hybrid Galerkin numerical modelling of elastodynamics and compressible Navier–Stokes couplings: applications to seismo-gravito acoustic waves

Quentin Brissaud,[1] Roland Martin,[2] Raphaël F. Garcia[1] and Dimitri Komatitsch[3]

[1] *Institut Supérieur de l'Aéronautique et de l'Espace (ISAE-SUPAERO), Université de Toulouse, Toulouse, France. E-mail: quentin.brissaud@isae.fr*
[2] *Laboratoire de Géosciences Environnement Toulouse (GET), UMR CNRS 5563, Observatoire Midi-Pyrénées, Université Paul Sabatier, Toulouse, France*
[3] *Aix Marseille Univ., CNRS, Centrale Marseille, LMA, Marseille, France*

Accepted 2017 May 3. Received 2017 March 28; in original form 2017 January 9

SUMMARY

We introduce a hybrid Galerkin modelling tool for the nonlinear acoustic and gravity wave propagation in planetary atmospheres coupled through topography to a solid medium. We rely on a 2-D spectral-element technique to model linear visco-elastic solid media and couple it to a discontinuous Galerkin method for the atmosphere modelled by the fully nonlinear Navier–Stokes equations. Significant benefits of such a method are, first, its versatility because it handles both acoustic and gravity waves in the same simulation, second, it enables one to observe nonlinear effects as convection or wave-breaking and, finally, it allows one to study the impact of ground-atmosphere coupling for waves propagating from seismic sources. Simulations are performed for 2-D isothermal atmosphere models with complex wind and viscosity profiles. We validate the computations by comparing them to finite-difference solutions, already validated in a previous paper. Specific benchmark validation cases are considered for both acoustic and gravity waves subject to viscosity variations, wind duct and nonlinear wave breaking. We apply this tool to study acoustic and gravity waves generated by a strong seismic source and its nonlinear breaking in the upper atmosphere.

Key words: Acoustic-gravity waves; Non-linear differential equations; Numerical modelling; Computational seismology; Earthquake ground motions; Wave propagation.

1 INTRODUCTION

Acoustic and gravity waves propagation in planetary atmospheres provide a way to probe their structure and dynamics but may also offer a window into the internal structure of the planet from the coupling between its fluid and solid parts. In order to better understand the propagation of these waves, many authors have worked on the modelling of linear or nonlinear propagation with different techniques that range from normal-mode computations to ray tracing by solving linearized Navier–Stokes equations or using global circulation models (Yiğit & Medvedev 2015, for a review). One of the motivations behind this work and a main difference between these techniques consists in accounting or not for nonlinear wave propagation. Studies relying on the linear assumption divide the atmospheric variables into slowly varying or stationary background parts and small first-order wave perturbations. A second type of study considers the whole system which implies the propagation of shocks, waves-waves interactions and the resulting transfers of energy and wave-breaking for large-amplitude waves. Many theoretical studies of acoustic and gravity waves have been done using the linear theory (Mikhailenko & Mikhailov 2014; Wei *et al.* 2015; Brissaud *et al.* 2016), since it provides a good understanding of waves dynamics for smooth atmospheric conditions (Dörnbrack & Nappo 1997). On Earth, in the middle and upper atmospheres, the background flows often approach these conditions, but in the troposphere and in the planetary boundary layer this approximation may break. For nonlinear propagation several methods can be used: finite-differences (Kshevetskii & Gavrilov 2005; de Groot-Hedlin 2016) present a great advantage in terms of simplicity of implementation but fail to resolve with good accuracy both strong background velocity fields and contact between different material. The finite volume method (Snively & Pasko 2008) addresses these two issues efficiently but lacks accuracy compared to high-order finite-element methods. Finally, finite elements offer great advantages, even though it is computationally more expensive than finite differences, in terms of accuracy and boundary conditions since it relies on a weak formulation. But it shows instabilities when dealing with strongly varying background (Hüppe *et al.* 2016). In this study, we use a discontinuous Galerkin (DG) method, common in fluid dynamics since it provides great accuracy with harsh background conditions, and efficiently takes into account boundary conditions (Hesthaven & Warburton 2007). Global circulation models, common in

atmospheric studies, are also based on the full Navier–Stokes equations but they also take into account several other factors such as humidity, clouds or rains (Miyoshi *et al.* 2014). Other less common methods have been used (Lecoanet *et al.* 2015) and give interesting results for specific applications. Different formulations are available for Navier–Stokes equations. Climatologists studying the atmosphere often use a temperature potential or temperature formulation (Ahmad & Lindeman 2007; Müller *et al.* 2010). But the total energy formulation tends to give more stable and less dissipative results than temperature formulations (Giraldo 1995). Another crucial point to understand the propagation of infrasounds from sources in the solid Earth up to the atmosphere is the coupling between those media. Many authors focused either on the atmosphere (Kshevetskii & Gavrilov 2005) or the solid medium (Komatitsch & Tromp 1999), respectively considering solid or free-surface boundary conditions for the solid-fluid boundary. In order to fully couple those media, several options are available: normal-mode techniques (Lognonné *et al.* 1998) take into account free oscillations of the Earth but are limited to a certain range of frequencies and are only 1-D. Most of the Euler or Navier–Stokes solutions, when considering fluid-solid coupling, focus on acoustic modes only and do not resolve gravity modes since they are mainly interested in ocean-Earth or more generally acoustic-elastic couplings (Komatitsch *et al.* 2000; Schäfer & Teschauer 2001; van Vossen *et al.* 2002; Käser & Dumbser 2008).

Regarding numerical aspects, when using the DG method, a numerical procedure is required to resolve discontinuities at element boundaries and also to stabilize the simulations when dealing with strong nonlinearities. The first aspect, the computations of fluxes at element boundaries and the associated Riemann problem, can be approximated in different ways: Roe, Lax-Friedrich or Harten-Lax-van Leer contact based fluxes are common examples but since we will not focus on strong shocks, or shock–shock interactions the choice is not significant and we will choose a simple, stable and efficient one: the Lax-Friedrich flux. The other aspect, for nonlinear stability, usually relies on slope-limiting techniques (Cockburn & Shu 2001). In our case we will again choose a relatively simple first-order 'flux-limiter' (Hesthaven & Warburton 2007) as it gives great results without a high computational cost.

Also, as mentioned earlier, to properly understand the propagation of acoustic and gravity waves due to atmospheric sources or seismic sources one should be able to properly model the Earth-Atmosphere system. Due to the high computational cost of the DG method we couple this method to a less expensive continuous Galerkin method (a spectral-element method) in the solid medium already available in the SPECFEM2D software package and that shares the same polynomial discretization as the DG method. Also, in order to validate the method in the fluid domain, we perform comparisons against a finite-difference method, already validated and published (Brissaud *et al.* 2016), which will provide solutions in complex atmospheric conditions.

In this paper, we first quickly recall the main equations for wave propagation in the fluid and the solid media as well as boundary and interface conditions. We then describe numerical aspects of both continuous and DG methods as well as the fluid-solid interface numerical treatment. Next, we present the different atmosphere and Earth models and validation results (acoustic and gravity waves and absorption under windy atmospheric conditions) against finite-difference solutions. Finally, we simulate post-seismic acoustic and gravity waves and analyse the associated nonlinear breaking.

2 SOLID AND FLUID EQUATIONS

In this section let us recall the different sets of equations for the propagation of acoustic and gravity waves for a viscous fluid and the propagation of compressional and shear waves in a solid medium, as well as the boundary and interface conditions required to close the fully coupled solid-fluid system. To limit the computational cost we will restrict the study to 2-D models and the work will need to be extended to 3-D models in future papers. We consider the following computation domains and boundaries:

(i) The solid (respectively fluid) interior domain Ω_S (respectively Ω_F)
(ii) The fluid–solid boundary Γ_{FS}
(iii) The solid outer boundary $\Gamma_{S,\,\mathrm{ext}}$
(iv) The fluid outer boundary $\Gamma_{F,\,\mathrm{ext}}$
(v) The solid boundary $\Gamma_S = \Gamma_{FS} \cup \Gamma_{S,\,\mathrm{ext}}$
(vi) The fluid boundary $\Gamma_F = \Gamma_{FS} \cup \Gamma_{F,\,\mathrm{ext}}$

We will also make the following assumptions:

(i) the atmosphere is a Newtonian fluid
(ii) the atmosphere is an ideal gas
(iii) the solid is an isotropic linear (i.e. we consider small elastic perturbations only) visco-elastic medium

2.1 Notations

Table 1 summarizes the variables, constants and notations used in the paper.

Table 1. The main variables, constants and notations used in our paper. Main variables have the following dimensions: ρ_T (kg m^{-3}), $\mathbf{v}_F$, $\mathbf{v}_S$ (m s^{-1}), e (J kg^{-1}), T (K), $\mathbf{g}$ (m s^{-2}), C_p, C_v (kg m^2 s^{-2} K^{-1}), κ (W K^{-1} m^{-1}), p (kg m^{-1} s^{-2}), μ (kg m^{-1} s^{-1}), c, $c_{S,p}$, $c_{S,s}$ (m s^{-1}), N (rad Hz), L_x, L_z, h (m).

Name	Meaning	Name	Meaning
Ω_F	Fluid domain	Ω_S	Solid domain
Γ_F	Fluid domain boundary	Γ_S	Solid domain boundary
$\Gamma_{F,\text{ext}}$	Fluid domain outer boundary	$\Gamma_{S,\text{ext}}$	Solid domain outer boundary
Γ_{FS}	Fluid–solid interface		
Ω_F^k	Curvilinear element of the fluid domain	$\partial\Omega_F^k$	Boundary of a curvilinear element
T	Temperature	ρ_S	Background seismic density
ρ	Total atmospheric density	e	Total energy per unit mass
$\mathbf{v}_F$	Total fluid velocity	$\mathbf{v}_{0,F}$, $\mathbf{v}_{1,F}$	Background and perturbation fluid velocities
p	Total atmospheric pressure	p_0, p_1	Background and perturbation atmospheric pressures
Σ_i	Inviscid fluid stress tensor	$\Sigma_{0,i}$, $\Sigma_{1,i}$	Background and perturbation inviscid fluid stress tensors
Σ_v	Viscous fluid stress tensor	$\Sigma_{0,v}$, $\Sigma_{1,v}$	Background and perturbation viscous fluid stress tensors
σ_e	Viscous fluid energy tensor	$\sigma_{0,e}$, $\sigma_{1,e}$	Background and perturbation viscous fluid energy tensors
T	Temperature	γ	Ratio of specific heat
μ	Dynamic viscosity	κ	Thermal conductivity
C_p	Heat capacity at constant pressure	C_v	Heat capacity at constant volume
c	Adiabatic sound velocity	L	Mean free path
$\mathbf{g}$	Gravitational acceleration	N	Brunt-Väisälä frequency
$\mathbf{v}_S$	Total solid velocity	$\mathbf{v}_{S,0}$, $\mathbf{v}_{S,1}$	Background and perturbation solid velocities
S_T	Total solid stress tensor	S_0, S	Background and perturbation solid stress tensors
ϵ_T	Total solid strain tensor	ϵ_0, ϵ	Background and perturbation solid strain tensors
$\mathbf{C}$	Total solid stiffness tensor	λ_S, μ_S	Lamé parameters
$c_{S,p}$	P-wave solid wave velocity	$c_{S,s}$	S-wave solid wave velocity
f_ρ, $\mathbf{f}_v$, f_e	Mass, momentum and energy fluid sources	$\mathbf{f}_S$	Solid source
$\mathbf{n} = (n_x, n_z)$	Unit normal to a surface	$\mathbf{t} = (t_x, t_z)$	Unit tangent vector to a surface
$\mathbf{v}_{F,NT}$	Fluid velocity projected in surface coordinates	$\tilde{\Sigma}_i$	Nonlinear fluid stress tensor
$\mathcal{L}$	Navier–Stokes and Elastodynamics operators		
L_x	Domain size along x	L_z	Domain size along z
Δt	Time step	Δx	Spatial step
P_T	Dominant time period of a source or a forcing	P_S	Dominant wavelength of a source or a forcing
t_0	Initial source or forcing time	A	Source or forcing amplitude (or incident wave angle in Section 4.4)
h	Topography height	T_v, R_v	Velocity transmission and reflexion coefficients
$\mathbf{F}_b$	Fluid bottom momentum forcing	f_b	$z-$component of the fluid bottom momentum forcing

2.2 Atmosphere modelled by the Navier–Stokes equations system

In the fluid domain, Navier–Stokes equations describe the nonlinear motion of viscous fluids. Various formulations exist for this nonlinear set of equations, the main difference lying in the choice of the last equation describing the energy balance from the state equation. Some authors, mainly in the climatology field, rely on the potential temperature (Shamarock *et al.* 2008; Müller *et al.* 2010) and others in the Computational Fluid Dynamics community use total energy as a conservative variable (Giraldo 1995; Bassi & Rebay 1997; Tang & Warnecke 2005; Chandrashekar & Zenk 2017). In our framework these formulations are similar, but considering total energy leads to less dissipative results (Giraldo & Restelli 2008), let us mention that when using alternative numerical methods, such as finite differences, pressure can also be used but the system is not conservative anymore (Kshevetskii & Gavrilov 2005).

Then constitutive variables will be the fluid density ρ (kg m^{-3}), the fluid velocity $\mathbf{v}$ (m s^{-1}) and the total energy per unit mass e (J kg^{-1}). Their evolution in time is described by three conservation equations: the conservation of mass, conservation of momentum and the conservation of energy.

These equations read, for any point in the fluid domain Ω_F and $\forall t > 0$,

$$\begin{aligned}
\partial_t \rho &= -\nabla.(\rho \mathbf{v}_F) + f_\rho, \\
\partial_t \rho\mathbf{v} &= -\nabla.\Sigma_i + \nabla.\Sigma_v + \rho\mathbf{g} + \mathbf{f}_v, \\
\partial_t \rho e &= -\nabla.(\{\rho e + p\}\mathbf{v}_F) + \rho\mathbf{g}.\mathbf{v}_F + \nabla.\sigma_e + f_e,
\end{aligned} \tag{1}$$

where $\mathbf{g}$ (m s^{-2}) is the gravity acceleration, $\gamma = \frac{C_p}{C_v}$ is the gas constant with C_p (kg m^2 s^{-2} K^{-1}) the heat capacity at constant pressure, and C_v the heat capacity at constant volume (kg m^2 s^{-2} K^{-1}), p the pressure (kg m^{-1} s^{-2}), f_ρ (kg m^{-3} s^{-1}) the mass source, $\mathbf{f}_v$ (kg m^{-2} s^{-2}) the momentum source, f_e (kg m^{-1} s^{-3}) the energy source and Σ_i (kg m^{-1} s^{-2}) is the inviscid fluid stress tensor that reads

$$\Sigma_i = \begin{pmatrix} \rho v_{F,x}^2 + p & \rho v_{F,x} v_{F,z} \\ \rho v_{F,x} v_{F,z} & \rho v_{F,z}^2 + p \end{pmatrix}. \tag{2}$$

Σ_v (kg m^{-1} s^{-2}) is the viscous fluid stress tensor and σ_e (kg s^{-3}) the viscous energy vector that read

$$\Sigma_v = \begin{pmatrix} (\eta_V - \frac{2}{3}\mu)\nabla.\mathbf{v}_F & \mu(\partial_x v_{F,z} + \partial_z v_{F,x}) \\ \mu(\partial_x v_{F,z} + \partial_z v_{F,x}) & (\eta_V - \frac{2}{3}\mu)\nabla.\mathbf{v}_F \end{pmatrix}, \quad \sigma_e = \mathbf{v}_F.\Sigma_v + \kappa\nabla T, \tag{3}$$

where μ (kg m^{-1} s^{-1}) is the shear viscosity. Atmospheric absorption can occur through two main mechanisms (Bass *et al.* 1984): losses due to dissipation of mechanical energy, and relaxation losses due to the conduction of heat energy. The shear (or dynamic) viscosity μ, due to shear stress applied to a fluid and relaxation of dilatational disturbances (i.e. viscous dissipation, heat conduction and molecular relaxations), reads (Zuckerwar & Ash 2006; Bass & Chambers 2001)

$$\mu = \frac{2}{3} L\rho c\sqrt{2/\pi\gamma}, \tag{4}$$

where L is the mean free path and c the adiabatic sound speed. The auxiliary variable η_V reads

$$\eta_V = \frac{4}{3}\mu. \tag{5}$$

Finally, T (K) is the temperature and κ (W K^{-1} m^{-1}) the thermal conductivity that describes the fluid ability to conduct heat. Temperature reads, from the expression of total energy e

$$T = \frac{1}{C_v}\left(e - \frac{1}{2}||\mathbf{v}_F||^2\right), \tag{6}$$

where $||.||$ is the $\mathbb{R}^2$ norm. Also, from the state equation (valid for the fluid considered as an ideal gas) follows a relationship between pressure and energy as

$$p = (\gamma - 1)\rho\left(e - \frac{1}{2}||\mathbf{v}_F||^2\right), \tag{7}$$

and eq. (6) yields

$$\frac{p}{\gamma - 1} = \rho C_v T. \tag{8}$$

2.3 Solid equations system: elastodynamics

For the solid Earth, we will consider a linear isotropic visco-elastic heterogeneous solid. The solution in the solid medium will rely on the small perturbation hypothesis, that is, the hypothesis that the background evolution in time can be neglected. Linear wave equations can then be written as (Komatitsch & Tromp 1999)

$$\rho_S \partial_t^2 \mathbf{u}_S = \nabla.S + \mathbf{f}_S, \tag{9}$$

with

$$\begin{aligned} S(t) &= \int_\infty^t \partial_t \mathbf{C}(t-\tau) : \epsilon(\tau) d\tau = \mathbf{C}^U : \epsilon - \sum_{m=1}^{L} \mathbf{R}^m \\ \partial_t \mathbf{R}^m &= -\mathbf{R}^m/\tau^{Sm} + \delta\mathbf{c}^m : \epsilon/\tau^{Sm} \\ \delta c^m_{ijkl} &= -C^R_{ijkl}\left(1 - \tau^{\epsilon m}_{ijkl}/\tau^{Sm}\right) \\ \epsilon &= \frac{1}{2}\left\{\nabla\mathbf{u}_S + (\nabla\mathbf{u}_S)^T\right\} \\ C_{ijkl} &= C^R_{ijkl}\left[1 - \sum_{m=1}^{L}\left(1 - \tau^{\epsilon m}_{ijkl}/\tau^{Sm}\right)e^{-t/\tau^{Sm}}\right]H(t), \\ C^U_{ijkl} &= C^R_{ijkl}\left[1 - \sum_{m=1}^{L}\left(1 - \tau^{\epsilon m}_{ijkl}/\tau^{Sm}\right)\right], \end{aligned} \tag{10}$$

where $\mathbf{u}_S$ (m) is the solid displacement, S (kg m^{-1} s^{-2}) is the solid stress tensor, ϵ (s^{-1}) is the strain rate tensor, $\mathbf{C}$ (kg m^{-1} s^{-1}) the stiffness tensor, λ_S and μ_S the Lamé parameters, ρ_S the solid density, $\mathbf{f}_S$ (kg m^{-2} s^{-2}) an external force, C^R_{ijkl}, C^U_{ijkl} denote respectively the relaxed and unrelaxed modulus, τ^{Sm} are the stress relaxation times (chosen to be the same for all components of the anelastic tensor), $\tau^{\epsilon m}_{ijkl}$ are the strain relaxation times (unique to each individual component of the anelastic tensor), L is the number of relaxation mechanisms and H is the Heaviside step function.

2.4 Boundary conditions and fluid–solid interface

One needs to provide boundary and interface conditions for both the solid medium and the fluid medium.

First, because we did not implement absorbing boundary conditions for the fluid medium yet we will take periodic boundary conditions on lateral boundaries (boundaries defined at $x = 0$ and $x = x_{\max}$ where $x_{\max}$ is the maximum x-coordinate for the simulation domain) for both fluid and solid media. If we denote by Γ_p the periodic boundaries we now consider the outer solid and fluid exterior boundaries as $\tilde{\Gamma}_{F,\text{ext}} = \Gamma_{F,\text{ext}} \setminus \Gamma_p$ and $\tilde{\Gamma}_{S,\text{ext}} = \Gamma_{S,\text{ext}} \setminus \Gamma_p$. In the following we will simplify the notation and remove the tilde by considering $\Gamma_{F,ext}$, $\Gamma_{S,ext}$ to be, respectively, the outer fluid and solid boundaries without the periodic boundaries.

For the fluid outer boundary conditions $\Gamma_{F,\text{ext}}$ we will consider perfect slip conditions, that is, the velocity field reads

$$\mathbf{v}_F.\mathbf{n} = \mathbf{0} \tag{11}$$

where $\mathbf{n} = (n_x \quad n_z)$ is the outer surface unit normal vector of $\Gamma_{F,\text{ext}}$ and $\mathbf{t} = (t_x \quad t_z)$ the unit tangent vector to the surface.

For the solid medium we impose wall boundary conditions on $\Gamma_{S,\text{ext}}$ such that all displacement perturbations will be zero at the boundary. However, the SPECFEM2D software allows for absorbing boundary conditions in elastic regions (Komatitsch & Tromp 2003).

At the fluid-solid boundary Γ_{FS} we consider a frictionless slip boundary condition (Aki & Richards 1980) which implies continuity of the traction and normal velocity across the surface and no mass transfer between the two domains

$$\begin{aligned} &\mathbf{v}_F.\mathbf{n} = \mathbf{v}_S.\mathbf{n} \\ &\Sigma_i.\mathbf{n} = S_T.\mathbf{n}, \end{aligned} \tag{12}$$

where $\mathbf{n}$ is the outer unit normal vector of the solid-fluid boundary Γ_{FS}.

2.5 Initial conditions: hydrostatic equilibrium

In order to close the system one should finally provide initial conditions. At the initial time we require hydrodynamic equilibrium, that is, no temporal variation of the initial atmospheric background, in order to prevent from possible extra spurious wave sources due to atmospheric instabilities. We thus focus on models that meet the following requirements

(i) Stratified models (no lateral spatial variations of atmospheric properties),
(ii) No initial vertical velocity field.

At the initial time, from eq. (1), constitutive equations then read:

$$\begin{aligned} \partial_z(\mu \partial_z v_{F,x}) &= 0 \\ \partial_z p &= -\rho g_z \\ \partial_z(\kappa \partial_z T) &= 0 \end{aligned} \tag{13}$$

Eq. (13) shows that any set of initial horizontal velocity field $v_{F,x}$ and if the viscosity tensor is diagonal (i.e. if one considers no shear viscosity μ but only bulk viscosity profiles η_V) and has no lateral variations is compatible with the hydrodynamic equilibrium. Also, eq. (13)-3 requires one to consider an adiabatic atmosphere with constant thermal conductivity or an isothermal atmosphere.

3 NUMERICAL METHOD

3.1 Discretization of Navier–Stokes and elastodynamics equations

We consider two numerical methods in order to solve the problem: The DG method to compute the numerical solution in the fluid domain and the continuous Galerkin method (CG), in its spectral form, in the solid domain. We implemented the DG method in the open-source SPECFEM2D software package (Komatitsch & Tromp 1999; Chaljub *et al.* 2007). Other authors have already investigated coupled continuous–discontinuous Galerkin methods for multi-phase flows (Landet *et al.* 2015), coupled Navier–Stokes and Darcy equations (Dawson 2008), fluid-structure interactions (Chidyagwai & Rivière 2010) or acousto-elastic waves (Ye *et al.* 2016), but the coupled Navier–Stokes and elastodynamics equations for acoustic and gravity wave propagation have not been implemented yet to the best of our knowledge.

3.1.1 Fluid domain: discontinuous spectral-element method

The fluid interior domain is discretized using the DG method (Kopriva *et al.* 2002; Kopriva 2006; Hesthaven & Warburton 2007). In order to construct the global approximation we decompose the domain Ω into non-overlapping curvilinear mesh elements such that,

$$\Omega_F = \cup_{k=1}^{N_e} \Omega_F^k, \tag{14}$$

where N_e is the number of elements and Ω_F^k a curvilinear mesh element with $\partial\Omega_F^k$ its boundary. We also define the 2-D reference element $I = [-1, 1]^2$ and introduce for each element $(\Omega_F^k)_{k=1,N_e}$ a smooth, bijective transformation $\mathcal{F}_{\Omega_F^k}(I) = \Omega_F^k$ (this assumes that the Jacobian of the mesh transformation is never singular which is a required condition when building a good-quality mesh). Also, for the sake of simplicity and for consistency with the continuous spectral-element method used in the solid domain, we will assume that the mesh is geometrically conforming. The transformation $\mathcal{F}_{\Omega_F^k}$ needs to be approximated by a polynomial mapping based on a set of N_c control nodes. For generic vectors Ψ and $\mathbf{Q}_k$ that lie, respectively, in I and Ω_F^k this mapping writes

$$\mathbf{Q}_k = \Psi \circ \mathcal{F}_{\Omega_F^k}^{-1}. \tag{15}$$

We introduce the set of Gauss–Lobatto–Legendre (GLL) points and then define a basis of $\mathcal{P}_N$ by considering the Lagrange interpolants $(h_i^N)_{i=1,N+1}$ at the GLL points, that is, the $N+1$ polynomials of order N that satisfy, $\forall(i,j) \in [1, N+1]^2$

$$h_i^N(\zeta_j) = \delta_{ij}. \tag{16}$$

In 2-D we define the Lagrange interpolants as $h_{ij}^N(\zeta) = h_i^N(\xi)h_j^N(\eta)$, where $\zeta = (\xi, \eta)$ is the generic coordinate vector associated with the reference element. We can now construct a polynomial basis $(\Psi_{ij})_{i=1,N+1;\, j=1,N+1}$ such that

$$\Psi_{ij} = h_{ij}^N, \quad i = 1, N+1 \quad j = 1, N+1. \tag{17}$$

Then, the mapping defined in eq. (15) now writes

$$\mathbf{Q}_k = \Psi \circ \mathcal{F}_{\Omega_F^k}^{-1} \approx \sum_{i=1}^{N+1}\sum_{j=1}^{N+1} \mathbf{Q}_k(\mathbf{x}_{ij})\Psi_{ij}\left(\mathcal{F}_{\Omega_F^k}^{-1}(\mathbf{x}_{ij})\right), \tag{18}$$

where $\mathbf{x}_{ij} = \mathcal{F}_{\Omega_F^k}(\zeta_{ij}) \in \Omega_F^k$, $i, j = 1, N+1$ are the control nodes coordinates.

We finally introduce the polynomial space for discretization $V_k = \{\Phi \in \mathbb{L}^2(\Omega_F) \cap \mathbb{H}^1(\Omega_F^k) : \Phi|_{\Omega_F^k} = \Psi \circ \mathcal{F}_{\Omega_F^k}^{-1}$, with $\Psi \in \mathcal{P}_N$, $k = 1, N_e\}$.

We numerically solve the system (1) for variables $\mathbf{Q} \in V_k^4$

$$\mathbf{Q} = \begin{pmatrix} \rho \\ m_x = \rho v_x \\ m_z = \rho v_z \\ E = \rho e \end{pmatrix}, \tag{19}$$

with the momentum vector $\mathbf{m}$ that reads $\mathbf{m} = (m_x, m_z)$. By multiplication of eq. (1) with a test function $\Phi \in V_k$ and after integration over an element Ω_F^k, we obtain

$$\begin{aligned}
\int_{\Omega_F^k} \partial_t \rho \Phi \mathrm{d}\Omega_k &= -\int_{\Omega_F^k} \nabla.(\rho \mathbf{v}_F)\Phi \mathrm{d}\Omega_k + \int_{\Omega_F^k} f_\rho \Phi \mathrm{d}\Omega_k, \\
\int_{\Omega_F^k} \partial_t \mathbf{m} \Phi \mathrm{d}\Omega_k &= -\int_{\Omega_F^k} \nabla.\Sigma_i \Phi \mathrm{d}\Omega_k + \int_{\Omega_F^k} \nabla.\Sigma_v \Phi \mathrm{d}\Omega_k + \int_{\Omega_F^k} \rho \mathbf{g} \Phi \mathrm{d}\Omega_k + \int_{\Omega_F^k} \mathbf{f}_v \Phi \mathrm{d}\Omega_k, \\
\int_{\Omega_F^k} \partial_t E \Phi \mathrm{d}\Omega_k &= -\int_{\Omega_F^k} \nabla.(\{\rho e + p\}\mathbf{v}_F)\Phi \mathrm{d}\Omega_k + \int_{\Omega_F^k} \nabla.\sigma_e \Phi \mathrm{d}\Omega_k + \int_{\Omega_F^k} \rho \mathbf{g}.\mathbf{v}_F \Phi \mathrm{d}\Omega_k + \int_{\Omega_F^k} f_e \Phi \mathrm{d}\Omega_k.
\end{aligned} \tag{20}$$

Then, by integration by parts,

$$\begin{aligned}
\int_{\Omega_F^k} \partial_t \rho \Phi \mathrm{d}\Omega_k &= \int_{\Omega_F^k} \rho \mathbf{v}_F.\nabla\Phi \mathrm{d}\Omega_k - \int_{\partial\Omega_F^k} \rho \mathbf{v}_F.\mathbf{n}\Phi \mathrm{d}\Gamma_k + \int_{\Omega_F^k} f_\rho \Phi \mathrm{d}\Omega_k, \\
\int_{\Omega_F^k} \partial_t \mathbf{m} \Phi \mathrm{d}\Omega_k &= \int_{\Omega_F^k} \Sigma_i.\nabla\Phi \mathrm{d}\Omega_k - \int_{\partial\Omega_F^k} \Sigma_i.\mathbf{n}\Phi \mathrm{d}\Gamma_k - \int_{\Omega_F^k} \Sigma_v.\nabla\Phi \mathrm{d}\Omega_k + \int_{\partial\Omega_F^k} \Sigma_v.\mathbf{n}\Phi \mathrm{d}\Gamma_k + \int_{\Omega_F^k} \rho \mathbf{g} \Phi \mathrm{d}\Omega_k + \int_{\Omega_F^k} \mathbf{f}_v \Phi \mathrm{d}\Omega_k, \\
\int_{\Omega_F^k} \partial_t E \Phi \mathrm{d}\Omega_k &= \int_{\Omega_F^k} \{\rho e + p\}\mathbf{v}_F.\nabla\Phi \mathrm{d}\Omega_k - \int_{\partial\Omega_F^k} \{\rho e + p\}\mathbf{v}_F.\mathbf{n}\Phi \mathrm{d}\Gamma_k - \int_{\Omega_F^k} \sigma_e.\nabla\Phi \mathrm{d}\Omega_k + \int_{\partial\Omega_F^k} \sigma_e.\mathbf{n}\Phi \mathrm{d}\Gamma_k \\
&\quad + \int_{\Omega_F^k} \rho \mathbf{g}.\mathbf{v}_F \Phi \mathrm{d}\Omega_k + \int_{\Omega_F^k} f_e \Phi d\Omega_k.
\end{aligned} \tag{21}$$

This can be written in terms of fluxes as

$$\int_{\Omega_F^k} \partial_t \mathbf{Q} \mathrm{d}\Omega_k = \int_{\Omega_F^k} F_i(\mathbf{Q}).\nabla\Phi \mathrm{d}\Omega_k - \int_{\partial\Omega_F^k} F_i^*(\mathbf{Q}).\mathbf{n}\Phi \mathrm{d}\Gamma_k + \int_{\Omega_F^k} F_v(\mathbf{Q}).\nabla\Phi \mathrm{d}\Omega_k - \int_{\partial\Omega_F^k} F_v^*(\mathbf{Q}).\mathbf{n}\Phi \mathrm{d}\Gamma_k + \int_{\Omega_F^k} \mathbf{G}\Phi \mathrm{d}\Omega_k + \int_{\Omega_F^k} \mathbf{f}_F \Phi \mathrm{d}\Omega_k, \tag{22}$$

where

$$\mathbf{G} = \begin{pmatrix} 0 \\ 0 \\ \rho g_z \\ \rho g_z v_{F,z} \end{pmatrix} \quad \mathbf{f}_F = \begin{pmatrix} f_\rho \\ f_{v_x} \\ f_{v_z} \\ f_e \end{pmatrix} \quad F_i = \begin{pmatrix} \rho v_{F,x} & \rho v_{F,z} \\ \rho v_{F,x}^2 + p & \rho v_{F,x} v_{F,z} \\ \rho v_{F,x} v_{F,z} & \rho v_{F,z}^2 + p \\ (\rho e + p) v_x & (\rho e + p) v_z \end{pmatrix} \tag{23}$$

and

$$F_v = \begin{pmatrix} 0 & 0 \\ \left(\eta_V - \frac{2}{3}\mu\right) \nabla.\mathbf{v}_F & \mu(\partial_x v_{F,z} + \partial_z v_{F,x}) \\ \mu(\partial_x v_{F,z} + \partial_z v_{F,x}) & (\eta_V - \frac{2}{3}\mu)\nabla.\mathbf{v}_F \\ v_{F,x}\left(\eta_V - \frac{2}{3}\mu\right) \nabla.\mathbf{v}_F + v_{F,z}\mu(\partial_x v_{F,z} + \partial_z v_{F,x}) + \kappa \partial_x T & v_{F,x}\mu\left(\partial_x v_{F,z} + \partial_z v_{F,x}\right) + v_{F,z}\left(\eta_V - \frac{2}{3}\mu\right) \nabla.\mathbf{v}_F) + \kappa \partial_z T \end{pmatrix}. \tag{24}$$

F_i^* and F_v^* denote the value of inviscid and viscous fluxes at the boundary.

Coupling between neighbouring elements is recovered by the interface flux F^* using the Lax-Friedrich approximation. This approach, even though slightly more dissipative than other techniques (e.g. Roe fluxes), works well for both subsonic and super-sonic wave propagation (Hesthaven & Warburton 2007). It reads, for any unknown $q_k \in V_k$ and element Ω_F^k

$$\int_{\partial\Omega_F^k} F^*.\mathbf{n} \mathrm{d}\Gamma_k \approx \int_{\partial\Omega_F^k} \left(\overline{F(q_k)}.\mathbf{n} - \frac{1}{2}\lambda[q_k] \right) \mathrm{d}\Gamma_k, \tag{25}$$

where $\overline{F(q_k)} = \frac{1}{2}(F(q_k^+) + F(q_k^-))$ is the average mean, $[q_k] = (q_k^+ - q_k^-)$ is the jump, and λ is the approximate local maximum linearized acoustic wave speed that reads

$$\lambda = \max_{s\in\{x^-,x^+\}} \left(||\mathbf{v}_F(s)|| + \sqrt{\left| \frac{\gamma p(s)}{\rho(s)} \right|} \right). \tag{26}$$

The '$-$' and '$+$' notations denote the interior and exterior states, and x^-, x^+ are the interior and exterior location along the element boundary Γ_k. Another technique is implemented for viscous terms: following Bassi & Rebay (1997) we use a local DG method. Instead of applying Galerkin identities to temperature and velocity gradients in viscous fluxes F_v in eq. (23), that method consists in using a two-step approach: first we introduce auxiliary variables by defining vector $\mathcal{T}$ and tensor $\mathcal{V}$ as

$$\mathcal{T} = \nabla T; \quad \mathcal{V} = \nabla \mathbf{v}_F. \tag{27}$$

By multiplication of eq. (27) with a test function $\Phi \in V_k^2$ and after integration by parts over an element Ω_F^k one obtains, for the temperature,

$$\int_{\Omega_F^k} \mathcal{T}.\Psi \mathrm{d}\Omega_F^k = \int_{\Omega_F^k} \nabla T.\Psi \mathrm{d}\Omega_F^k = -\int_{\Omega_F^k} T \nabla.\Psi \mathrm{d}\Omega_F^k + \int_{\partial\Omega_F^k} T\Psi.\mathbf{n} \mathrm{d}\Gamma_k, \tag{28}$$

The same holds for the fluid velocity $\mathbf{v}_F$. Note that for viscous numerical fluxes, that do not represent wave propagation, we only take the average between left and right state at the boundary.

Next, after solving eq. (28), it consists in injecting $\mathcal{T}$ and $\mathcal{V}$ in viscous fluxes from eq. (24).

Finally, we use a classical total variation diminishing limiting technique called 'MUSCL' (Monotone Upstream-centred Scheme for Conservation Laws, refer to e.g. LeVeque 2002) in order to avoid spurious oscillations coming from shock propagation (details in Section 3.4).

3.1.2 Solid domain: continuous spectral-element method

We use, in the solid part, a classical continuous Galerkin SEM (e.g. Chaljub *et al.* 2007) with the same polynomial space V_h as in the fluid domain. Let us only recall here the main discretized equations. From eq. (9), by multiplication with a test function $\Phi \in V_h$ and after integration over the domain Ω_S, one obtains

$$\int_{\Omega_S} \rho_S \partial_t \mathbf{v}_S \Phi \mathrm{d}\Omega = \int_{\Omega_S} \nabla.S\Phi \mathrm{d}\Omega + \int_{\Omega_S} \mathbf{f}_S \Phi \mathrm{d}\Omega. \tag{29}$$

By integration by parts one obtains

$$\begin{aligned} \int_{\Omega_S} \rho_S \partial_t \mathbf{v}_S \Phi \mathrm{d}\Omega &= -\int_{\Omega_S} S.\nabla\Phi \mathrm{d}\Omega + \int_{\Gamma_S} S.\mathbf{n}\Phi \mathrm{d}\Gamma + \int_{\Omega_S} \mathbf{f}_S \Phi \mathrm{d}\Omega \\ &= -\int_{\Omega_S} S.\nabla\Phi \mathrm{d}\Omega + \int_{\Gamma_{FS}} S.\mathbf{n}\Phi \mathrm{d}\Gamma + \int_{\Gamma_{S,\mathrm{ext}}} S.\mathbf{n}\Phi \mathrm{d}\Gamma + \int_{\Omega_S} \mathbf{f}_S \Phi \mathrm{d}\Omega. \end{aligned} \tag{30}$$

We enforce rigid boundary conditions at the exterior solid boundaries $\Gamma_{S,\,\mathrm{ext}}$:

$$\int_{\Omega_S} \rho_S \partial_t \mathbf{v}_S \Phi \mathrm{d}\Omega = -\int_{\Omega_S} S.\nabla\Phi \mathrm{d}\Omega + \int_{\Gamma_{FS}} S.\mathbf{n}\Phi \mathrm{d}\Gamma + \int_{\Omega_S} \mathbf{f}_S \Phi \mathrm{d}\Omega. \tag{31}$$

Note that the memory variable equation (10)-2 is a simple ODE that will be only updated in time and does not require a Galerkin discretization.

3.2 Fluid–solid interfaces

The strategy to take into account the coupling between the Earth and the atmosphere consists in imposing perturbations of traction and velocity on both sides of the interface using boundary integrals. The coupling strategy from the solid to the fluid requires a few more steps than from the fluid to the solid because one needs to constrain the energy and the tangential velocity at the boundary.

3.2.1 Fluid to solid

The treatment of mechanical boundary conditions is similar to that in Komatitsch *et al.* (2000) and consists in imposing the stress at the boundary, as described in eq. (12), such that

$$\int_{\Gamma_{FS}} S_T.\mathbf{n}\Phi \mathrm{d}\Gamma = \int_{\Gamma_{FS}} (-\Sigma_i + \Sigma_v).\mathbf{n}\Phi \mathrm{d}\Gamma. \tag{32}$$

We recall that in the solid medium we solve only for linear perturbation and thus we recast eq. (31) in terms of perturbations

$$\int_{\Gamma_{FS}} S.\mathbf{n}\Phi \mathrm{d}\Gamma = \int_{\Gamma_{FS}} (-\Sigma_{1,i} + \Sigma_{1,v}).\mathbf{n}\Phi \mathrm{d}\Gamma. \tag{33}$$

The whole solid system (10) thus reads,

$$\int_{\Omega_S} \rho_S \partial_t \mathbf{v}_S \Phi \mathrm{d}\Omega = -\int_{\Omega_S} S.\nabla\Phi \mathrm{d}\Omega + \int_{\Gamma_{FS}} (-\Sigma_{1,i} + \Sigma_{1,v}).\mathbf{n}\Phi \mathrm{d}\Gamma + \int_{\Omega_S} \mathbf{f}\Phi \mathrm{d}\Omega. \tag{34}$$

3.2.2 Solid to fluid

At the solid-fluid boundary one needs to enforce mass, momentum and energy fluxes in eq. (21) from the boundary conditions specified in eq. (12). Note that this boundary condition involves the whole velocity and pressure fields, but as the equations in the solid medium will be solved in terms of small perturbations, we need to specify the conditions upon those perturbations. As long as the propagation in the fluid and close to the surface is linear we can also rely on the perturbation method near the fluid-solid interface. We thus split the fluid fields in mean and perturbation as

$$\begin{aligned} \mathbf{v}_F &= \mathbf{v}_{0,F} + \mathbf{v}_{1,F} \\ \Sigma_i &= \Sigma_{0,i} + \Sigma_{1,i}. \end{aligned} \tag{35}$$

We also consider the total fluid stress tensor $\Sigma_T = \Sigma_{0,\,T} + \Sigma_{1,\,T}$ as

$$\begin{aligned} \Sigma_T &= -\Sigma_i + \Sigma_v \\ \Sigma_{0,T} &= -\Sigma_{0,i} + \Sigma_{0,v}. \end{aligned} \tag{36}$$

With these notations the condition (12) reads

$$\begin{aligned} \mathbf{v}_F.\mathbf{n} &= \mathbf{v}_S.\mathbf{n} \\ \Sigma_T &= (\Sigma_{0,T} + \Sigma_{1,T}).\mathbf{n} = (S_0 + S).\mathbf{n}. \end{aligned} \tag{37}$$

The system being at equilibrium at the initial time, there is no initial velocity field in the solid medium ($\mathbf{v}_{0,S} = \mathbf{0}$) and tractions are balanced between the fluid and solid media ($\Sigma_{0,T}.\mathbf{n} = S_0.\mathbf{n}$). We also consider no fluid velocity field at the initial time near the fluid-solid interface, that is, near $\Gamma_{FS}\mathbf{v}_F = \mathbf{v}_{1,F}$. Therefore,

$$\begin{aligned} \mathbf{v}_F.\mathbf{n} &= \mathbf{v}_S.\mathbf{n} \\ \Sigma_{1,T}.\mathbf{n} &= S.\mathbf{n}. \end{aligned} \tag{38}$$

The mass flux on the fluid-solid boundary Γ_{FS} is straightforward to enforce because there is no mass transfer between the media and thus

$$(\rho \mathbf{v}_F.\mathbf{n})|_{\Gamma_{FS}} = (\rho \mathbf{v}_S.\mathbf{n})|_{\Gamma_{FS}} \tag{39}$$

The momentum fluxes will be enforced using the continuity of the traction across the boundary such that, from eq. (37),

$$(\Sigma_T.\mathbf{n})|_{\Gamma_{FS}} = (S_0 + S).\mathbf{n}|_{\Gamma_{FS}} = (\Sigma_{0,T} + S).\mathbf{n}\big|_{\Gamma_{FS}}. \tag{40}$$

From the condition (12) it is possible to determine the velocity at the boundary such that,

$$\mathbf{v}_{F,NT} = A\mathbf{v}_F \Leftrightarrow A^{-1}\mathbf{v}_{NT} = \mathbf{v}_F, \tag{41}$$

where $\mathbf{v}_{F,NT}$ is the fluid velocity projected on the normal $\mathbf{n}$ and tangential $\mathbf{t}$ directions along the boundary. A is the transformation matrix between Cartesian coordinates and fluid-solid interface coordinates

$$A = \begin{pmatrix} n_x & n_z \\ t_x & t_z \end{pmatrix} \quad A^{-1} = \frac{1}{n_x t_z - t_x n_z}\begin{pmatrix} t_z & -n_z \\ -t_x & n_x \end{pmatrix}. \tag{42}$$

The normal-tangential velocity vector is given by the boundary condition such that

$$\mathbf{v}_{F,NT} = \begin{pmatrix} \mathbf{v}_S.\mathbf{n} \\ \mathbf{v}_F.\mathbf{t} \end{pmatrix}_{NT}. \tag{43}$$

Finally, for the energy flux we need to find a value for the pressure perturbation at the interface. Indeed, at the boundary the energy flux reads

$$\{(\rho e + p)\mathbf{v}_F + \sigma_e\}.\mathbf{n}|_{\Gamma_{FS}} = \{(\rho e + p)\mathbf{v}_F + \Sigma_v.\mathbf{v}_F + \kappa\nabla T\}.\mathbf{n}|_{\Gamma_{FS}}. \tag{44}$$

Since at the fluid-solid interface the temperature is continuous and as the heat flux is negligible under the assumptions made for the solid medium in Section 2 we will neglect the heat flux at the boundary $\nabla T|_{\Gamma_{FS}} = 0$, eq. (44) reads

$$\{(\rho e + p)\mathbf{v}_F + \Sigma_v.\mathbf{v}_F + \kappa\nabla T\}.\mathbf{n}|_{\Gamma_{FS}} = \{(\rho e + p)\mathbf{v}_F + \Sigma_v.\mathbf{v}_F\}.\mathbf{n}|_{\Gamma_{FS}}. \tag{45}$$

Expanding the total energy in terms of pressure, density and velocity, one has

$$\begin{aligned}\{(\rho e + p)\mathbf{v}_F + \Sigma_v.\mathbf{v}_F + \kappa\nabla T\}.\mathbf{n}|_{\Gamma_{FS}} &= \left\{\left(\frac{p}{\gamma - 1} + \frac{\rho}{2}||\mathbf{v}_F||^2 + p\right)\mathbf{v}_S.\mathbf{n} + (\Sigma_v.\mathbf{v}_F).\mathbf{n}\right\}\Big|_{\Gamma_{FS}} \\ &= \left\{\left(\frac{\gamma}{\gamma - 1}p + \frac{\rho}{2}||\mathbf{v}_{F,NT}||^2\right)\mathbf{v}_S.\mathbf{n} + (\Sigma_v.\mathbf{v}_F).\mathbf{n}\right\}\Big|_{\Gamma_{FS}}.\end{aligned} \tag{46}$$

The only remaining unknown is the pressure, which we will enforce with the continuity of the traction. We first define the nonlinear stress tensor $\tilde{\Sigma}_i$

$$\tilde{\Sigma}_i = \rho\begin{pmatrix} v_{F,x}^2 & v_{F,x}v_{F,z} \\ v_{F,x}v_{F,z} & v_{F,z}^2 \end{pmatrix}. \tag{47}$$

Using the notation defined in eq. (47), the total stress tensor now reads: $\Sigma_i = p\mathbf{I} + \tilde{\Sigma}_i$. Then, from eq. (37)

$$\begin{aligned}\Sigma_T.\mathbf{n} &= (\Sigma_{0,T} - \Sigma_{1,i} + \Sigma_{1,v}).\mathbf{n} = (S_0 + S).\mathbf{n} \\ -\Sigma_{1,i}.\mathbf{n} &= (S - \Sigma_{1,v}).\mathbf{n} \\ (p_1\mathbf{I} + \tilde{\Sigma}_{1,i}).\mathbf{n} &= (-S + \Sigma_{1,v}).\mathbf{n} \\ p_1\mathbf{n} &= (-S - \tilde{\Sigma}_{1,i} + \Sigma_{1,v}).\mathbf{n} \\ \mathbf{n}^T.(p_1\mathbf{n}) &= \mathbf{n}^T.(-S - \tilde{\Sigma}_{1,i} + \Sigma_{1,v}).\mathbf{n} \\ p_1 &= \mathbf{n}^T.(-S - \tilde{\Sigma}_{1,i} + \Sigma_{1,v}).\mathbf{n}.\end{aligned} \tag{48}$$

Note that the viscous and nonlinear stress tensor Σ_v and $\tilde{\Sigma}_{1,i}$ are known at the boundary Γ_{FS} since they only depend on the fluid velocity $\mathbf{v}_F$, which is known from eq. (43).

Numerically, we impose weakly these boundary conditions in the DG formulation (22). As the propagation within the solid medium is linear we remove the jump across the interface in eq. (25) such that

$$\int_{\partial\Omega_F^k\cap\Gamma_{FS}} F^*.\mathbf{n}\mathrm{d}\Gamma_k = \int_{\partial\Omega_F^k\cap\Gamma_{FS}} \frac{1}{2}(F|_{FS^-} + F|_{FS^+}).\mathbf{n}\mathrm{d}\Gamma_k, \tag{49}$$

where $F|_{FS}^-$ is the flux at the fluid-solid boundary prescribed from the solid medium by eqs (39)–(40)–(47)–(48) and $F|_{FS}^+$ is the interior flux at the fluid-solid boundary coming from the fluid domain.

3.3 Time discretization

In order to march the solution in time with a certain level of accuracy and enforce the Total Variation Diminishing (TVD) property (Hesthaven & Warburton 2007) we use a fifth-order strong stability preserving Runge–Kutta scheme (Spiteri & Ruuth 2002) that reads, for any constitutive variable $\mathbf{v}$

$$\begin{cases} \mathbf{v}^{(0)} = 0;\ \tilde{\mathbf{v}}^{(0)} = 0, \\ \tilde{\mathbf{v}}^{(i)} = \alpha_i \tilde{\mathbf{v}}^{(i-1)} + \Delta t \mathcal{L}(\tilde{\mathbf{v}}^{(i-1)}), \\ \mathbf{v}^{(i)} = \mathbf{v}^{(i-1)} + \beta_i \tilde{\mathbf{v}}^{(i)}, \\ \mathbf{v}^{n+1} = \mathbf{v}^{(5)}. \end{cases} \tag{50}$$

with $\tilde{\mathbf{v}}$ an auxiliary variable and coefficients $(\alpha_i)_{i=1,5}$ and $(\beta_i)_{i=1,5}$ read

$$\begin{cases} i & 1 & 2 & 3 & 4 & 5 \\ \alpha_i & = 0 & -0.418 & -1.1922 & -1.6978 & -1.5142 \\ \beta_i & = 0.1497 & 0.3792 & 0.823 & 0.6995 & 0.1531 \end{cases}, \tag{51}$$

where $\mathcal{L}$ denotes the Navier–Stokes and elastodynamics operators and Δt the time step.

3.4 Slope-limiting procedure

Let us quickly recall the formulation of the solutions at the interfaces given by the slope-limiting procedure in a 1-D case. The reader can refer to Hesthaven & Warburton (2007) for more details. We first define the minmod function m as

$$m(a_1, a_2, a_3) = \begin{cases} s * \min_{1\leq i\leq 3} |a_i|, & |s| = 1 \\ 0, & \text{otherwise} \end{cases}, \tag{52}$$

with $s = \frac{1}{3}\sum_{i=1}^{m} \text{sign}(a_i)$. This minmod function defined in eq. (52) is zero except if the three arguments have the same sign. In this case, the function will return the smallest of the three arguments with the sign defined by s. If the three arguments are taken as the slope of the solution in neighbouring elements, the minmod function will be zero when the signs of the slopes are not the same (different signs indicate that there is an oscillation), and otherwise return the smallest slope. The minmod function acts as a problem identifier and also a slope limiter. From the minmod function we define interface fluxes as

$$\begin{aligned} v_l^k &= \overline{u}_h^k - m\left(\overline{u}_h^k - u_l^k, \overline{u}_h^k - \overline{u}_h^{k-1}, \overline{u}_h^{k+1} - \overline{u}_h^k\right), \\ v_r^k &= \overline{u}_h^k - m\left(u_r^k - \overline{u}_h^k, \overline{u}_h^k - \overline{u}_h^{k-1}, \overline{u}_h^{k+1} - \overline{u}_h^k\right), \end{aligned} \tag{53}$$

where v_l^k and v_r^k are left and right interface solutions that respect the Total Variation Diminishing in the Mean (TVDM, e.g. in Chapter 5 in Hesthaven & Warburton 2007) properties, u_h^k is the discretized solution at element k, $\overline{u}_h^k$ the mean of solution u_h^k on the element k, u_l^k and u_r^k the left and right values of the solution and h is the distance between the centre of two neighbouring elements. For sufficiently small time steps Δt these solutions satisfy the TVDM properties. Considering a first-order slope limiter one assumes that the solution reads

$$u_h^k(x) = \overline{u}_h^k + \left(x - x_0^k\right) \partial_x u_h^k, \tag{54}$$

where x_0 is the location of the centre of element k. Then, in order to satisfy eq. (53) on the interfaces one defines the first-order slope limited solution as

$$\Pi_1 u_h^k(x) = \overline{u}_h^k + \left(x - x_0^k\right) m\left(\partial_x u_h^k, \frac{\overline{u}_h^k - \overline{u}_h^{k-1}}{h/2}, \frac{\overline{u}_h^{k+1} - \overline{u}_h^k}{h/2}\right). \tag{55}$$

In our case we consider a more stable but dissipative approach given by the classic MUSCL limiter (LeVeque 2002) that writes

$$\Pi_1 u_h^k(x) = \overline{u}_h^k + \left(x - x_0^k\right) m\left(\partial_x u_h^k, \frac{\overline{u}_h^k - \overline{u}_h^{k-1}}{h}, \frac{\overline{u}_h^{k+1} - \overline{u}_h^k}{h}\right). \tag{56}$$

In addition to avoid applying the slope limiter and in order to prevent from applying the limiting (but numerically dissipative) procedure in smooth regions, in which we would then lose accuracy, we apply the following procedure:

(1) Compute interface values (v_l^k, v_r^k) of the solution following eq. (53),

(2.a) If we have $(v_l^k, v_r^k) \approx (u_h^k(x_l^k), u_h^k(x_r^k))$ then there is no need for limiting the solution (This is strictly equal because it is dependent on the numerical scheme accuracy),

(2.b) Otherwise, we break the TVDM property and then limit the solution using eq. (56) and thus replacing $u_h^k(x)$ by its limited value $\Pi_1 u_h^k(x)$.

Table 2. Constant parameters of the isothermal model: from left to right, surface density, scale height, gravity, sound speed, square of the Brunt-Väisälä frequency, acoustic cut-off angular frequency, ratio of heat capacities, and temperature. We use a constant molar mass of 28.96 g mol^{-1}.

	ρ_0 (kg m^{-3})	H (km)	g_z (m s^{-2})	c (m s^{-1})	N^2 ($\frac{\text{rad}^2}{s^2}$)	w_c (rad s^{-1})	γ (no unit)	T (°K)
Model 1	1	8.417	9.81	340	3.3×10^{-4}	0.0202	1.4	287.5
Model 2	0.4	29	9.831	631	10^{-4}	0.011	1.4	1000

Finally, to reduce the loss of accuracy around local extrema we modify the minmod function following Shu (1987) as

$$\overline{m}(a_1, a_2, a_3) = m(a_1, a_2 + Mh^2 \operatorname{sign}(a_2), a_3 + Mh^2 \operatorname{sign}(a_3)). \tag{57}$$

where M is a constant that represents the upper bound of the second derivative at the local extrema. This constant M can be hard to select in practice because too small values gives the classical minmod function, while too large values reintroduce the oscillations that have been removed by the slope limiter. Based on empirical tests not shown here we set $M = 0.05$.

4 BENCHMARK CASES AND APPLICATIONS TO ACOUSTIC AND GRAVITY WAVES

Let us first validate our DG method against finite-difference solutions already validated and published in Brissaud *et al.* (2016). By doing so we can validate simulations in complex atmospheric cases even though no analytical solutions are available. That finite-difference code is based on a linear approach with a small perturbation approximation and thus will be useful only for smooth background conditions and low amplitude waves. However it takes into account gravity, attenuation and horizontal wind variations with altitude. We thus use this validation process only for linear solutions in a domain without any coupling with the Earth nor topography since the finite-difference code does not account for these issues. Finally, we added in Appendices A and B other benchmark test results of typical fluid dynamics problems produced by our modelling tool.

4.1 Atmosphere and Earth physical models

Let us simulate wave propagation in several atmosphere models. We will design an isothermal model to test the stability of the calculations relative to the exponential density decrease in the atmosphere. We will then build a more realistic model coming from empirical data with only vertical variations of the parameters.

4.1.1 Isothermal model

We first create a model where air density and pressure decrease exponentially with a constant scale height, all other parameters being constant. The values of these parameters are representative of those observed in the low-atmosphere ('Model 1') and the thermosphere ('Model 2') and are summarized in Table 2. The model is built assuming an ideal gas in hydrostatic equilibrium at constant temperature (Nappo 2002) and thus satisfies the hydrostatic equilibrium eqs (13).

4.1.2 Realistic atmosphere model

In order to verify the stability of our calculations relative to realistic vertical variations of atmospheric parameters, we create a model that exhibits only vertical variations of the bulk viscosity profile that is extracted from the MSISE-00 atmosphere model (Picone *et al.* 2002), and from the HWM93 atmospheric wind model (Hedin 1991). The thermodynamic properties of the atmospheric compounds are taken from the NIST web-book data base (Linstrom & Mallard 2015, http://webbook.nist.gov/chemistry, retrieved 31 May 2017). We extracted a vertical viscosity and wind profile for conditions corresponding to a surface point at latitude 36.5°, longitude 158.7° at 7:47:40 UTC on March 11, 2011. This space and time location corresponds to the coordinates of the crossing between the post-seismic infrasonic waves generated by the Tohoku earthquake in Japan and the GOCE satellite (Garcia *et al.* 2013).

We still face three limitations in the construction of atmosphere models. First, when one considers a coupled solid-atmosphere simulation with a non-flat topography, and if the initial horizontal atmosphere velocity field is non-zero at the boundary, the wind acts as a constant force against the solid medium and continuously generates seismic waves. This happens because we do not build a proper boundary layer at the fluid-solid interface. Second, since realistic models, as the MSISE−00 model, are empirical models they do not honour hydrostatic constrains at initial time specified in Section 2.5. This means that a filtering procedure is required on the initial density field to avoid generating instabilities. Then, from eq. (13) the density at the initial time must verify

$$\rho = \frac{\partial_z p}{g_z}. \tag{58}$$

With the initial pressure field provided by the empirical atmosphere model we then compute a new density profile that honours the hydrostatic equilibrium. This works well for low altitude simulations but gives very low densities that are close to the numerical scheme error at altitudes

Table 3. Simulation parameters corresponding to Model 2 from Section 4.1.1 for Simulation 4.2, that is, the case of a plane-wave 'high-frequency' forcing in a viscous atmosphere with exponentially decaying density.

$L_x \times L_z$ (km)	Δx (m)	Δt (s)	ρ (kg m^{-3})	c (m s^{-1})	μ (kg m^{-1} s^{-1})	κ (W K^{-1} m^{-1})	g_z (m s^{-2})	$v_{F,x}$ (m s^{-1})
1×280	100	5.10^{-3}	Varying	631	3/4	0	9.831	0

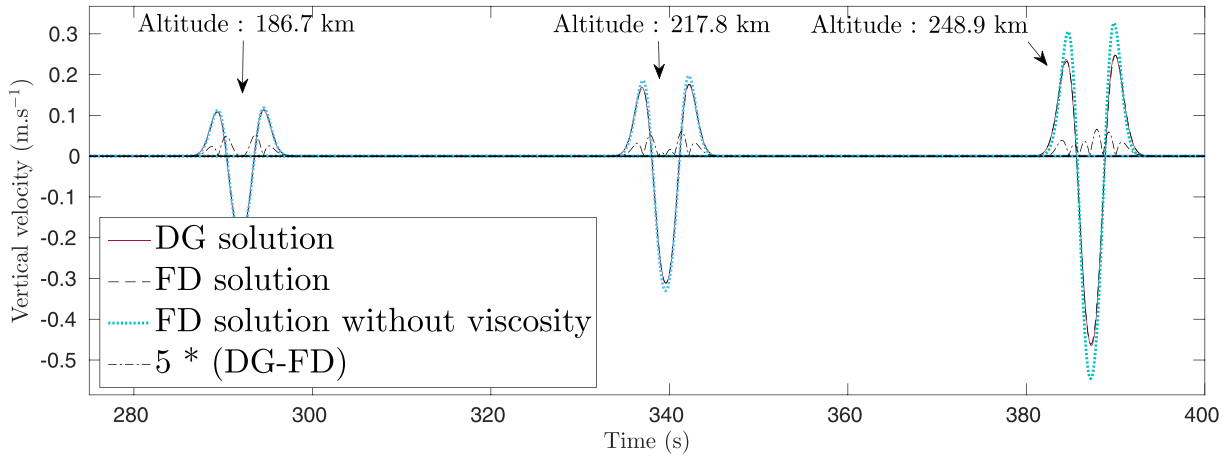

Figure 1. Vertical velocity for the finite-difference solution ('FD solution') and without viscosity ('FD solution without viscosity') and the discontinuous Galerkin solution ('DG solution') as well as the difference between the two multiplied by a factor 5 ('5*(DG-FD)'). The signals are shown through time for Simulation 4.2, that is, the case of a plane-wave 'high-frequency' forcing in a viscous atmosphere with exponentially decaying density. The comparison is shown at the three recording stations located at the same $x = 0.3$ km, their position along z being, from left to right, $z = 186.7$, 217.8 and 248.9 km. The atmosphere is considered isothermal (Table 3).

above 150 km, which leads to instabilities. These two points should be investigated in more details in future work. Finally, as one can note in eq. (13), if there is an initial horizontal velocity field, in order to get hydrostatic equilibrium at the initial time, the shear viscosity and thermal conductivity must be constants or 'compensate' the vertical variations of the initial velocity. Thus, we will only consider the diagonal elements of the viscous stress tensor Σ_v in eq. (1). The MSISE-00 model provides the thermal conductivity, from which we compute the bulk viscosity (that accounts for thermal relaxation). Thermal effects being taken into account by the bulk viscosity, we will thus take in this case $\kappa = 0$.

4.2 Plane-wave 'high-frequency' forcing in a viscous atmosphere with exponentially decaying density

The first validation concerns attenuation processes (both volume and shear viscosity). We consider a high-frequency spatially uniform forcing, $\forall \mathbf{x} \in \Gamma_{FS}$:

$$f(\mathbf{x}, t) = A \left(e^{-\left[\frac{t-(t_0-P_T/4)}{P_T/4}\right]^2} - e^{-\left[\frac{t-(t_0+P_T/4)}{P_T/4}\right]^2} \right), \tag{59}$$

where $P_T = 6$ s is the dominant time period of the forcing signal, $t_0 = 6$ s is the starting forcing time and the forcing amplitude is $A = 0.01$ m s^{-1}. The atmosphere is described by Model 2 in Section 4.1.1 and summarized in Table 3. Let us now compare numerical and analytical particle velocities at several recording stations.

Fig. 1 shows recorded vertical velocity at various altitudes at the same x location. One notes a good agreement in terms of phase and amplitude between the finite-difference and the DG simulations, with a maximum relative error of less than 5 per cent.

4.3 Bottom 'low-frequency' forcing in an atmosphere with exponentially decaying density

In order to study and validate gravito-acoustic wave propagation and the underlying physical processes, we consider the forcing function, $\forall \mathbf{x} \in \Gamma_{FS}$:

$$f(\mathbf{x}, t) = \left(e^{-\left[\frac{t-(t_0-P_T/4)}{P_T/4}\right]^2} - e^{-\left[\frac{t-(t_0+P_T/4)}{P_T/4}\right]^2} \right) \left(e^{-\frac{x-(x_0-P_S/4)^2}{P_S/4}} - e^{-\frac{x-(x_0+P_S/4)^2}{P_S/4}} \right), \tag{60}$$

where $P_T = 400$ s is the dominant time period of the forcing signal, $P_S = 20$ km is the dominant wavelength along x, $t_0 = 450$ s is the starting forcing time, and $x_0 = 75$ km is the position of the bottom forcing along x. The atmosphere is described by Model 1 in Section 4.1.1 and summarized in Table 4 with Brunt-Väisälä squared frequency $N^2 = 3.3 \times 10^{-4}$ rad^2 s^{-2}. We perform a windy simulation for which we set a

Table 4. Simulation parameters corresponding to Model 1 from Section 4.1.1 for Simulation 4.3, that is, the case of a bottom 'low-frequency' forcing in an atmosphere with exponentially decaying density with a wind duct.

$L_x \times L_z$ (km)	Δx (m)	Δt (s)	ρ (kg m^{-3})	c (m s^{-1})	μ (kg m^{-1} s^{-1})	κ (W K^{-1} m^{-1})	g_z (m s^{-2})	$v_{F,x}$ (m s^{-1})
150 × 37.5	250	10^{-2}	Varying	340	$(3/4)10^{-5}$	0	9.81	Varying

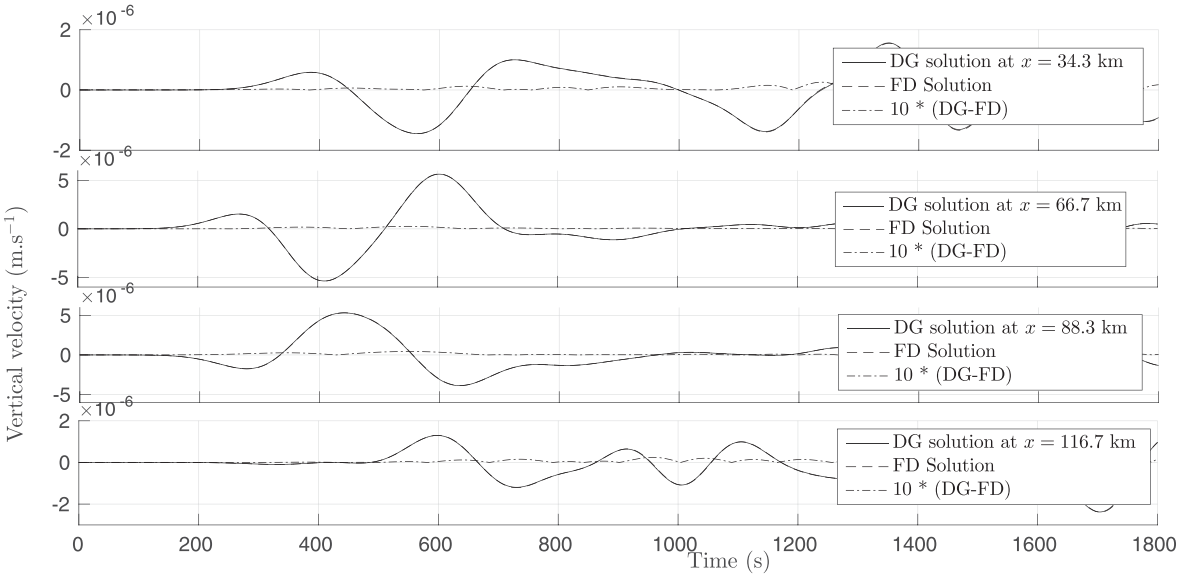

Figure 2. Vertical velocity for the finite-difference ('FD solution') and the discontinuous Galerkin solutions ('DG solution') as well as the difference between the two multiplied by a factor 10 ('10*(DG-FD)'). The signals are shown through time for Simulation 4.3, that is, the case of a bottom 'low-frequency' forcing in an atmosphere with exponentially decaying density with a wind duct. The comparison is shown at the four recording stations located at the same altitude $z = 10$ km, their position along x being, from top to bottom, $x = 34.3$, 66.7, 88.3 and 116.7 km. The atmosphere is considered isothermal (Table 4).

sinusoidal initial background wind as, at $t = 0$

$$v_{F,x}(\mathbf{x}, 0) = 100 \sin\left(\frac{2\pi z}{37500}\right). \tag{61}$$

Let us compare DG and FD particle velocities at several recording stations for a simulation with a strong background wind.

Fig. 2 shows recorded vertical velocity at various locations along the same altitude. One notes a good agreement in terms of phase and amplitude between the finite-difference and DG simulations, with a maximum relative error of less than 2 per cent. One can also note the impact of the Doppler shift on gravity wave propagation: upwind waves have a larger period and larger amplitude than downwind ones. Again, the results show a very good agreement in terms of vertical velocity against the finite-difference solution. Fig. 3 presents snapshots of the DG simulation. A typical feature of gravity wave propagation can be observed: the group and phase velocities are orthogonal.

4.4 Plane wave transmission/reflection from ground to atmosphere

In order to validate the fluid-solid coupling over a hilly terrain, we propagate a plane wave from the solid Earth up to the atmosphere and compare wave amplitudes using the analytical reflection and transmission coefficients.

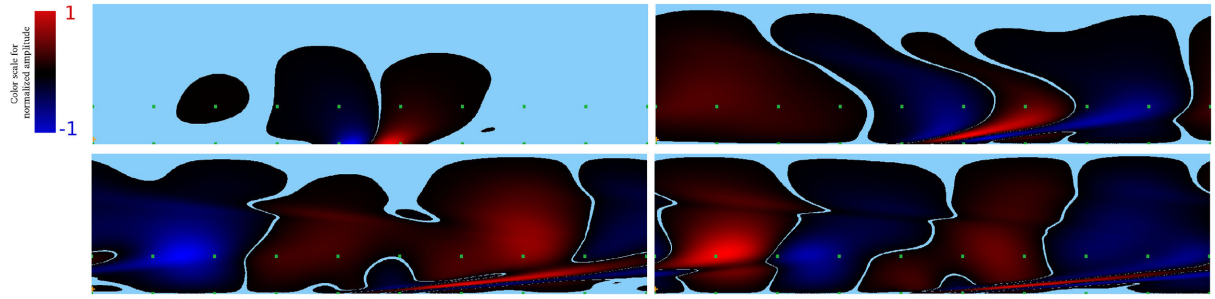

Figure 3. Snapshots of vertical velocity for the discontinuous Galerkin solution for Simulation 4.3, that is, the case of a bottom 'low-frequency' forcing in an atmosphere with exponentially decaying density with a wind duct. Snapshots are shown, on the top, from left to right, at times $t = 400$, 800 and, on the bottom, from left to right, at times $t = 1110$, 1213 s. Red colours indicate positive vertical velocities and blue colours negative ones. The green squares show the location of the recording stations. The atmosphere is considered isothermal (Table 4).

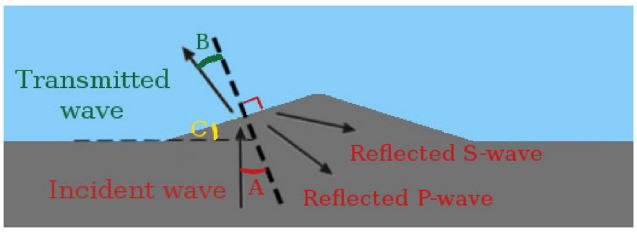

Figure 4. Topography for Simulation 4.4, that is, the case of a plane wave transmission/reflection from ground to atmosphere. Blue corresponds to the fluid medium and grey to the solid medium. A, B and C are respectively the incident and transmitted waves angles, and topography angle. The arrows show the direction of propagation of waves, and the dashed lines are the normal to the surface and the line along the flat terrain.

Table 5. Simulation parameters corresponding to Model 1 from Section 4.1.1 for Simulation 4.4, that is, the case of a plane wave transmission/reflection from ground to atmosphere.

Fluid	$L_x \times L_z$ (km)	Δx (m)	Δt (s)	ρ (kg m^{-3})	c (m s^{-1})	μ (kg m^{-1} s^{-1})	κ (W K^{-1} m^{-1})	g_z (m s^{-2})	$v_{F,x}$ (m s^{-1})
	$6.4 \times 2.4 - h(x)$	89	5.10^{-3}	1	340	0	0	0	0
Solid	$L_x \times L_z$ (km)	Δx (m)	Δt (s)	ρ	$c_{S,p}$	$c_{S,s}$	Q	f_0	–
	$6.4 \times 2.4 + h(x)$	89	5.10^{-3}	2500	3400	1963	0	0	–

To do so we consider a spatially uniform forcing $\mathbf{F}_b = f_b \mathbf{e}_z$ (kg m^{-1} s^{-2}), $\forall x \in \Gamma_S$, $t > 0$

$$f_b(\mathbf{x}, t) = -2\left[\frac{1}{P_T/4}\right]\left[\frac{t-(t_0+P_T/4)}{P_T/4}\right]e^{-\left[\frac{t-(t_0-P_T/4)}{P_T/4}\right]^2} + 2\left[\frac{1}{P_T/4}\right]\left[\frac{t-(t_0+P_T/4)}{P_T/4}\right]e^{-\left[\frac{t-(t_0+P_T/4)}{P_T/4}\right]^2}, \tag{62}$$

where the dominant time period is $P_T = 0.5$ s and the starting time is $t_0 = 0.5$ s. This forcing is introduced as a stress such that from eq. (31)

$$\int_{\Omega_S} \rho_S \partial_t \mathbf{v}_S \Phi \mathrm{d}\Omega = -\int_{\Omega_S} S.\nabla\Phi \mathrm{d}\Omega + \int_{\Gamma_{FS}} S.\mathbf{n}\Phi \mathrm{d}\Gamma + \int_{\Gamma_S} \mathbf{F}_b.\mathbf{n}\Phi \mathrm{d}\Gamma. \tag{63}$$

We will also consider a triangle-shaped topography h, $\forall x \in \Gamma_S$

$$h(x) = \begin{cases} \frac{h_{\max}}{x_2 - x_1}(x - x_1) & \text{if } x_2 > x >= x_1 \\ \frac{h_{\max}}{x_2 - x_3}(x - x_3) & \text{if } x_3 > x >= x_2 \end{cases}, \tag{64}$$

where $h_{\max} = 500$ m, $x_1 = 1600$ m and $x_2 = 3200$ m. In order to validate the numerical simulations we analytically compute expected amplitudes of transmitted and reflected waves depending on the wave incidence angle.

Fig. 4 shows the incidence wave angle A and transmitted wave angle B relative to the surface inclination. From the angle C, the inclination of the topography, we can easily find the incidence angle A such that $A = C$. Following eq. (64) we find $A = \arctan(\frac{h_{\max}}{x_2 - x_1}) = 0.5586$ rad. Using Snell's law we compute the cosine of angle B as

$$\cos(B) = \sqrt{1 - \frac{c^2}{c_{S,p}^2}\sin^2 A}, \tag{65}$$

where $c_{S,p}$ is the P-wave velocity in the solid medium. Now, from Aki & Richards (1980), we find velocity transmission T_v and reflexion R_v coefficients as

$$\begin{cases} T_v = \frac{2\rho c_{S,p}\cos A}{\rho_S C_p \cos B + \rho c \cos A} \\ R_v = \frac{\rho c \cos A - \rho_S c_{S,p}\cos B}{\rho_S c_{S,p}\cos B + \rho c \cos A} \end{cases}. \tag{66}$$

Thus for normal incidence ($A = 0$) we obtain $T_v = 1.9999$ and $R_v = 0.9999$ and for oblique incidence ($A = 0.5586$, $\cos(B) = 0.9986$) we get $T_v = 1.6983$.

Let us now compare the amplitude of the numerical solutions to analytical amplitudes using eq. (66) at several recording stations for a simulation in an homogeneous solid and fluid. The atmosphere is described by Model 1 in Section 4.1.1 and summarized in Table 5.

Fig. 5 shows the propagation, at different times, of incident P-wave and reflected P and S waves in the solid as well as acoustic wave fronts in the fluid. One notes normal and oblique plane wave fronts propagating respectively over flat and oblique terrains. We also note spherical waves propagating from the sharp corners of the topography because these ground irregularities act as point sources from the Huygens principle, that is, act as diffraction points. Also, due to the wave speed contrast, waves in the fluid domain have smaller wavelength than in the solid.

Table 6. Simulation parameters corresponding to Model 2 from Section 4.1.1 for Simulation 4.5, that is, the case of the validation of the contact discontinuity for nonlinear acoustic waves: the shock tube test.

$L_x \times L_z$ (km)	Δx (m)	Δt (s)	ρ (kg m^{-3})	c (m s^{-1})	μ (kg m^{-1} s^{-1})	κ (W K^{-1} m^{-1})	g_z (m s^{-2})	$v_{F,x}$ (m s^{-1})
4×1	0.01	10^{-3}	Varying	Varying	0	0	0	0

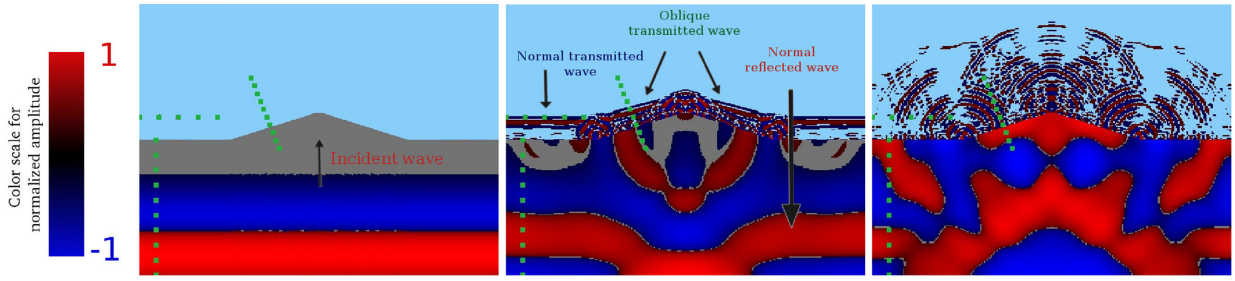

Figure 5. Snapshots of vertical velocity for the discontinuous Galerkin solution for Simulation 4.4, that is, the case of a plane wave transmission/reflection from ground to atmosphere with a wind duct. Snapshots are shown, from left to right, at time $t = 0.6$, 2.1 and 6 s. Fluid and solid vertical velocities are normalized separately. Red colours indicate positive vertical velocities and blue colours negative ones. The green squares show the location of the recording stations. The atmosphere is considered isothermal (Table 5).

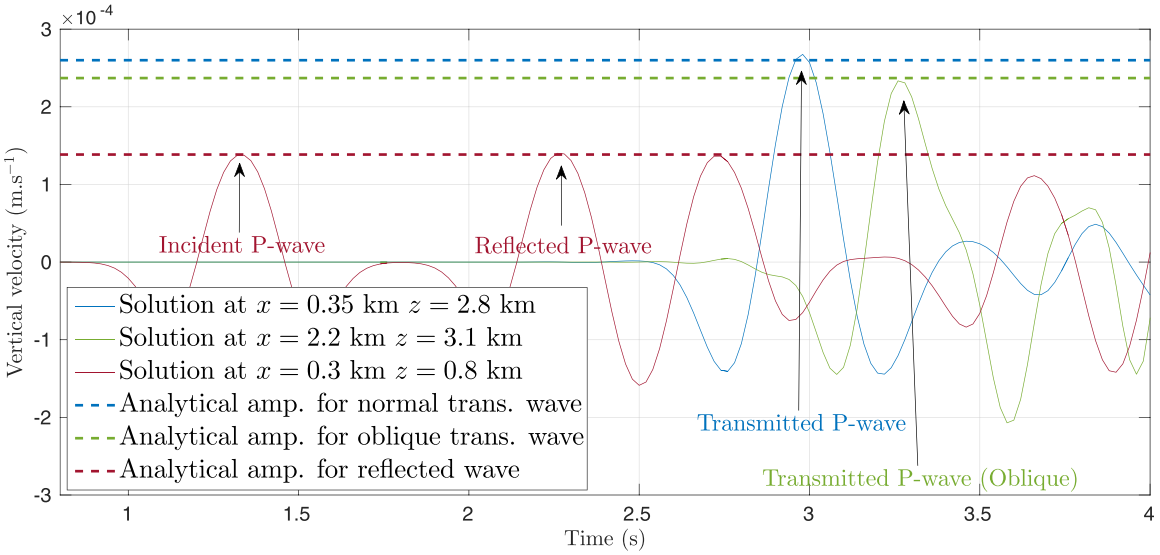

Figure 6. Vertical velocity for the discontinuous Galerkin solution ('Solution') at various locations to observe normal transmitted waves, oblique transmitted waves as well as reflected waves and it also shows analytical amplitudes computed using eq. (66) for normal transmitted waves ('Analytical amp. for normal trans. wave' using T_v with $A = 0$), oblique transmitted waves ('Analytical amp. for oblique trans. wave' using T_v with $A = 0.5586$ rad) and reflected waves ('Analytical amp. for reflected wave' using R_v with $A = 0$). The signals are shown through time for Simulation 4.4, that is, the case of a plane wave transmission/reflection from ground to atmosphere. The comparison is shown at three recording stations located, at $(x, z) = (0.35, 2.8)$ km, $(x, z) = (2.2, 3.1)$ km and $(x, z) = (0.3, 0.8)$ km. The atmosphere is considered isothermal (Table 5).

Fig. 6 shows signals of transmitted and reflected *P*-waves through time. The DG method with topography gives good results in terms of maximum expected amplitude for oblique and normal transmission.

4.5 Validation of the contact discontinuity for nonlinear acoustic waves: the shock tube test

This validation case, called the Sod's shock tube test, first proposed by Sod (1978) corresponds to the generation of shock waves due to density contrast between two fluids. Initial density and pressure profiles can be found in Kursungecmez (2015), and the exact solution is given in Whitham (2011). At the initial time $t = 0$ s, pressure and density read

$$p = \begin{cases} 1 & \text{if } x > 0.5 \\ 0.1 & \text{if } x \leq 0.5 \end{cases}$$
$$\rho = \begin{cases} 1 & \text{if } x > 0.5 \\ 0.125 & \text{if } x \leq 0.5 \end{cases}. \tag{67}$$

This initial state in eq. (67) can be produced by having a diaphragm in the middle of the tube. The gas to the left and right of the diaphragm is initially at rest. The pressure and density are discontinuous across the diaphragm. At $t = 0$ s, the diaphragm is broken. An expansion wave and two types of singularities then propagate through the tube. The initial simulation setup is given by eq. (67) and summarized in Table 6.

Fig. 7 shows that the initial discontinuity in (67) develops into a left moving expansion wave, right moving shock wave and right going contact discontinuity. One notes that numerical dissipation smooths out the contact surface since we only use a first-order slope limiter. But

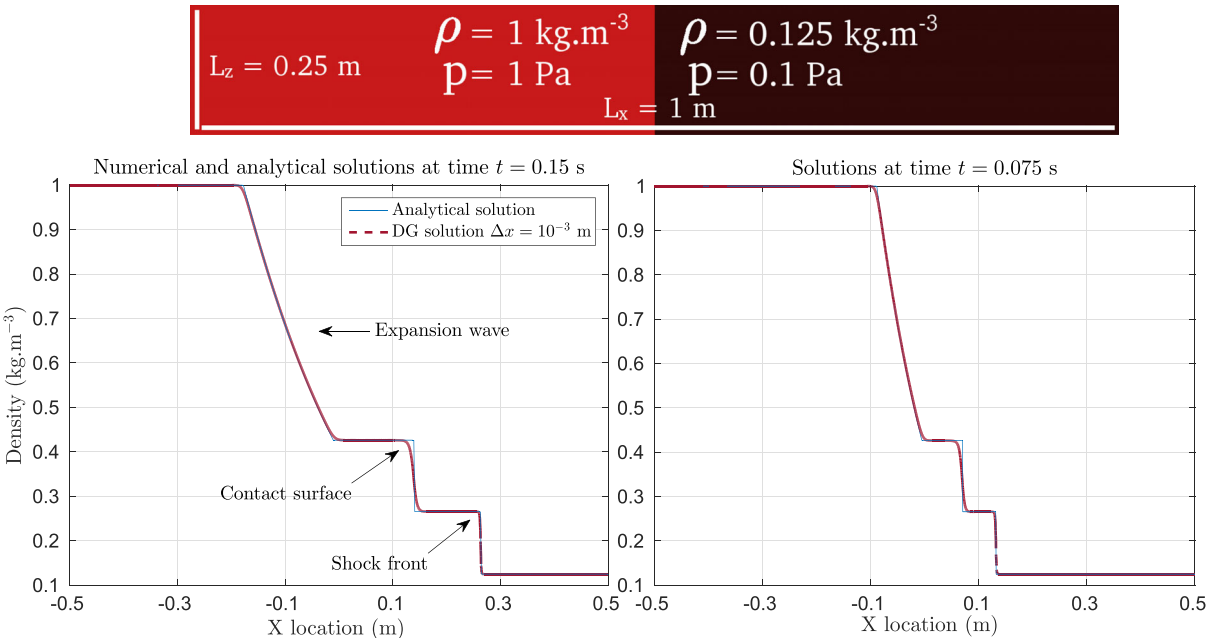

Figure 7. On the top, domain configuration at initial time for Simulation 4.5, that is, the case of a validation of the contact discontinuity for nonlinear acoustic waves: the shock tube test. The high density fluid is represented on the left in red and the low density one in dark-red colour. On the bottom, density signals for the DG simulation. The signals are shown along x for Simulation 4.5, that is, the case of a validation of the contact discontinuity for nonlinear acoustic waves: the shock tube test. The comparison is shown at two times $t = 0.075$ and 0.15 s and along x for same location $z = 0.01$ m. The atmosphere is considered isothermal (Table 6).

Table 7. Simulation parameters corresponding to Model 2 from Section 4.1.1 for Simulation 5.1, that is, the case of nonlinear acoustic waves.

$L_x \times L_z$ (km)	Δx (m)	Δt (s)	ρ (kg m^{-3})	c (m s^{-1})	μ (kg m^{-1} s^{-1})	κ (W K^{-1} m^{-1})	g_z (m s^{-2})	$v_{F,x}$ (m s^{-1})
5 × 300	100	5.10^{-3}	Varying	631	$(3/4)10^{-4}$	0	9.831	0

because we do not focus on strong shocks, and since there is a trade-off between computation time and accuracy for the slope limiter, the efficiency of the first order slope limiter is sufficient for our applications.

5 APPLICATIONS TO ACOUSTIC AND GRAVITY WAVES PROPAGATION

5.1 Nonlinear acoustic waves

In this subsection we study nonlinear acoustic wave fronts created by strong vertical velocity bottom forcing. We run a simulation similar to that in Section 4.2, but we increase the bottom forcing amplitude in eq. (59), using $A = 10$ m s^{-1}. The atmosphere is described by Model 2 in Section 4.1.1 and summarized in Table 7.

This test demonstrates the numerical method capability to take into account acoustic wave breaking in the atmosphere and measure the experimental limit of linear theory applied to acoustic and gravity wave propagation. In Fig. 8, as the amplitude gets stronger the wave packet slowly distorts (see the signal at the station located at $z = 96.6$ km) leading to a typical 'saw-toothed' shape and, finally, a N-wave shock (Whitham 2011) whereas in the finite-difference linear code the wave front amplitude only increases as the wave propagates in the atmosphere. This should be investigated in a more realistic model in future work because it seems to show that infrasounds can break for low Mach numbers. One also notes Gibbs oscillations in the vicinity of discontinuities due to lack of spatial resolution, but since viscosity is non-zero, they are damped through time.

5.2 Strong seismic wave

We study the propagation of a strong seismic wave from the ground to the atmosphere due to a moment tensor source. We rely on a simple isothermal stratified model and focus on shocks and seismic-generated gravity waves. We will show two simulations results, one with a seismic source located close to the surface in the solid to focus on gravity waves and a second one with a source located deeper in the solid to investigate acoustic shocks. We will first consider a flat fluid-solid interface located at $z = 10$ km over a rectangular domain of dimensions $L_x = 400$ km and $L_z = 100$ km. We consider a moment-tensor source as

$$\mathbf{f}_S = -M.\nabla\delta(\mathbf{x} - \mathbf{x}_S)G(t), \tag{68}$$

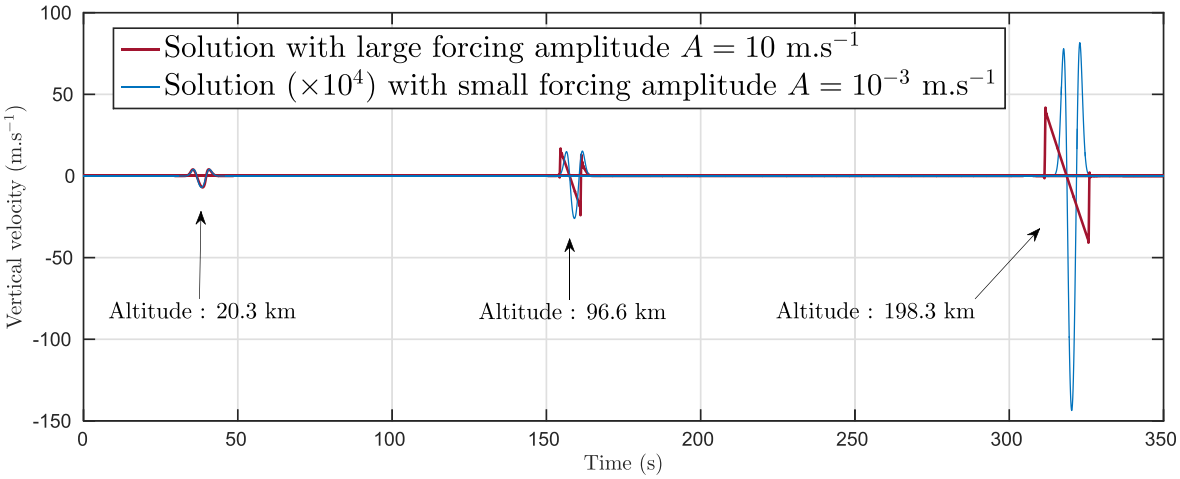

Figure 8. Vertical velocity for the discontinuous Galerkin solution for the large forcing amplitude simulation ('Solution with large forcing amplitude') and the small forcing amplitude simulation ('Solution ($\times$ 10^4) with small forcing amplitude'). The small forcing simulation signal is multiplied by 10^4 in order to see on the same plot both small and large amplitude forcing results. The signals are shown through time for Simulation 5.1, that is, the case of nonlinear acoustic waves. The comparison is shown at the three recording stations located at the same $x = 0.3$ km location, their position along z being, from left to right, $z =$ 20.3, 96.6 and 198.3 km. The atmosphere is considered isothermal (Table 7).

Table 8. Simulation parameters corresponding to Model 1 from Section 4.1.1 for Simulation 5.2, that is, the case of a strong seismic wave.

Fluid	$L_x \times L_z$ (km)	Δx (m)	Δt (s)	ρ (kg m^{-3})	c (m s^{-1})	μ (kg m^{-1} s^{-1})	κ (W K^{-1} m^{-1})	g_z (m s^{-2})	$v_{F,x}$ (m s^{-1})
	400 × 90	1000	0.05	varying	340	$(3/4)10^{-5}$	0	9.81	0
Solid	$L_x \times L_z$ (km)	Δx (m)	Δt (s)	ρ	$c_{S,p}$	$c_{S,s}$	Q	f_0	–
	400 × 10	1000	0.05	2500	3400	1963	1	0.05	–

where δ is the Dirac delta distribution located at $\mathbf{x}_s = (200, 2)$ km, M is a moment tensor

$$M = \begin{pmatrix} 0 & 1 \\ 1 & 0 \end{pmatrix}, \tag{69}$$

and G the source time function

$$G(t) = Ae^{-\alpha(t-t_0)^2}, \tag{70}$$

with $A = 10^{16}$ N m, $\alpha = (\pi f_0)^2$ and $t_0 = \frac{1.2}{f_0}$. We consider a low-frequency source having $f_0 = 2 \times 10^{-2}$ Hz. The atmosphere is described by Model 1 in Section 4.1.1 and summarized in Table 9 with Brunt-Väisälä squared frequency $N^2 = 3.3 \times 10^{-4}$ rad^2 s^{-2}.

In Fig. 9, one notes that the strong seismic source generates both acoustic and gravity waves. Acoustic wave fronts propagate first from the solid-fluid interface location right above the source as spherical wave fronts and, as seismic waves propagate in the solid medium, they generate oblique acoustic wave fronts in the atmosphere. Also, right above the seismic source atmospheric gravity waves are generated due to the long-period ground displacements induced by the low-frequency components of the source excitation.

Fig. 10 shows, for the low-frequency source simulation, both acoustic wave fronts ('Main acoustic wave-front'), at two recording stations, and the low-frequency gravity wave that is well visible in the 'filtered' signal (filtered with a low-pass Butterworth filter with a cut-off frequency of $f_0 = 5 \times 10^{-4}$ Hz). The main acoustic wave-front arrival is prior to the main seismic arrival because the location along x of the recording station is closer to the source in the fluid ($x = 204$ km) than in the solid domain ($x = 214$ km). Secondary seismic wave fronts, and their acoustic counter-parts, of 50 s period and visible at $t = 250, 480$ s are due to lateral periodic boundary conditions.

We now turn to the study of acoustic shocks by showing in Fig. 11 the results of two simulations, one with a low amplitude source from eq. (68) with $A = 10^{16}$ N m and another one with a relatively large amplitude source, with $A = 10^{18}$ N m. Both source time functions have the same dominant frequency $f_0 = 2 \times 10^{-2}$ Hz. The domain is still rectangular but we consider a fluid-solid interface located at $z = 100$ km and a larger solid medium in order to set the source deeper in the ground, at $(x, z) = (100, 25)$ km.

Table 9. Simulation parameters corresponding to Model 1 from Section 4.1.1 for Simulation 5.2, that is, the case of a plane wave transmission/reflection from ground to atmosphere.

Fluid	$L_x \times L_z$ (m)	Δx (m)	Δt (s)	ρ (kg m^{-3})	c (m s^{-1})	μ (kg m^{-1} s^{-1})	κ (W K^{-1} m^{-1})	g_z (m s^{-2})	$v_{F,x}$ (m s^{-1})
	200 × 100	1000	0.05	varying	340	$(3/4)10^{-5}$	0	9.81	0
Solid	$L_x \times L_z$ (km)	Δx (m)	Δt (s)	ρ	$c_{S,p}$	$c_{S,s}$	Q	f_0	–
	200 × 100	1000	0.05	2500	3400	1963	1	0.05	–

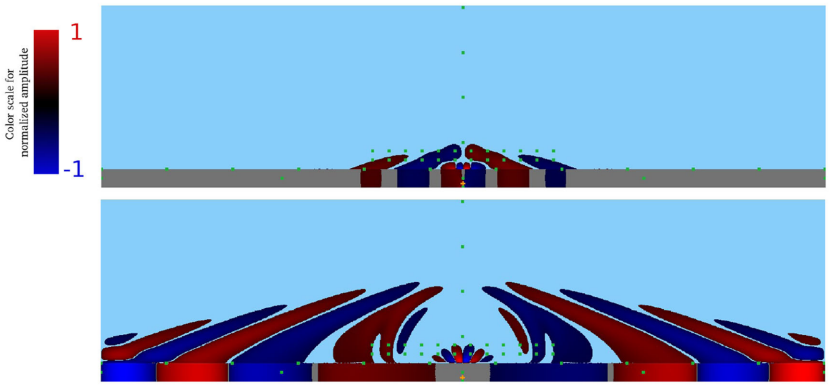

Figure 9. Snapshots of density-scaled vertical velocity ($\sqrt{\rho}v_z$) for the discontinuous Galerkin solution for Simulation 5.2, that is, the case of a strong seismic wave. Snapshots are shown, from top to bottom, at time $t = 75$ and 180 s. Figures show simulation run with a low-frequency source $f_0 = 2 \times 10^{-2}$ Hz. Fluid and solid vertical velocities are normalized separately. Red colours indicate positive vertical velocities and blue colours negative ones. The green squares show the location of the recording stations. The yellow square is the source location. The atmosphere is considered isothermal (Table 8).

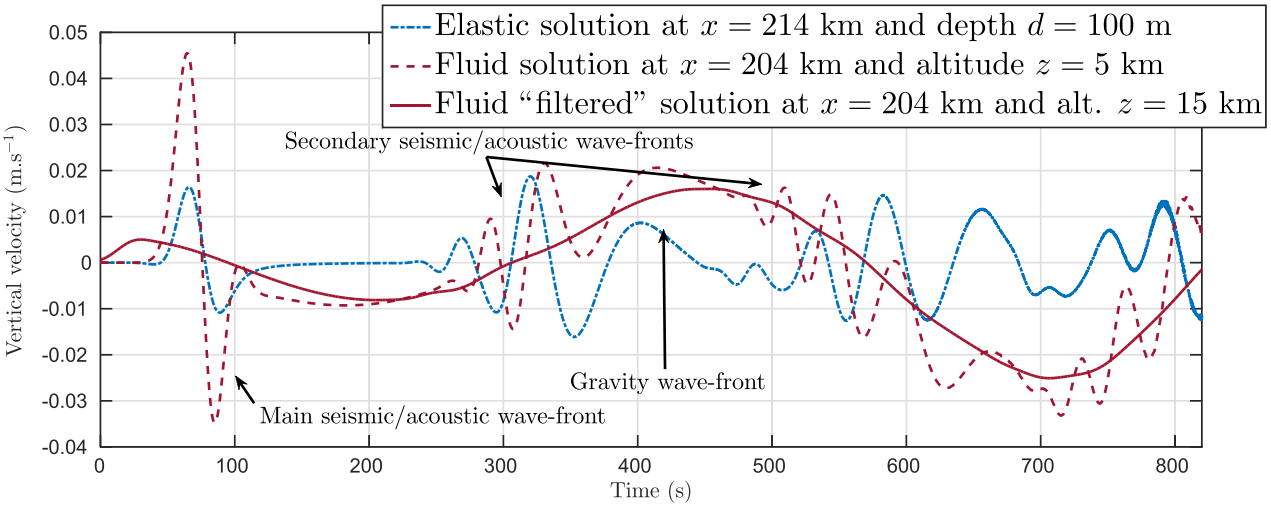

Figure 10. Vertical velocity for the discontinuous Galerkin solution for the low-frequency source $f_0 = 2 \times 10^{-2}$ Hz at a single depth in the solid medium ('Elastic solution') and different altitudes in the atmosphere ('Fluid solution'). The Figure also shows the fluid solution filtered to keep low frequencies only ('Fluid 'filtered' solution'). The signals are shown through time for Simulation 5.2, that is, the case of a strong seismic wave. The comparison is shown at two recording stations located, in the fluid, at $(x, z) = (204, 15)$ km and, in the solid medium, at $(x, z) = (214, 9.9)$ km. The atmosphere is considered isothermal (Table 8).

The right panel of Fig. 11 shows that, for a large-amplitude moment source, a strong wave is generated in the fluid that distorts and breaks as it propagates with altitude. It generates an unstable region in the fluid right above the seismic source shown by the loss of symmetry and the generation of an *N*-wave. This is clearly visible in the bottom of Fig. 11 where the solution for the large amplitude source shows the shock wave front generation through time. These results suggest that, since a shock is still visible at time 150 s and 60 km altitude, the formation of nonlinear acoustic *N*-waves from bottom seismic forcing may appear above the source region of earthquakes of relatively low magnitudes (Moment magnitude 6.0 in this case). However, such hypothesis will need to be validated even further in future work by 3-D simulations and with finite sources in realistic atmosphere models.

5.3 Nonlinear gravity waves

Let us now focus on the breaking of gravity waves due to strong wind shear or convective instabilities, which has been intensively studied in Kshevetskii & Gavrilov (2005). This will help showing that our technique can correctly handle nonlinear effects induced by gravity wave propagation.

We consider the following vertical velocity bottom forcing, $\forall t > 0$ and $x \in \Gamma_{FS}$

$$v_{F,z} = \begin{cases} -A \sin \omega(t - \frac{x}{c}) \exp(-(F(t - t_0))^2) & \text{if } t \leq t_0 \\ -A \sin \omega(t - \frac{x}{c}) & \text{if } t > t_0 \end{cases} \tag{71}$$

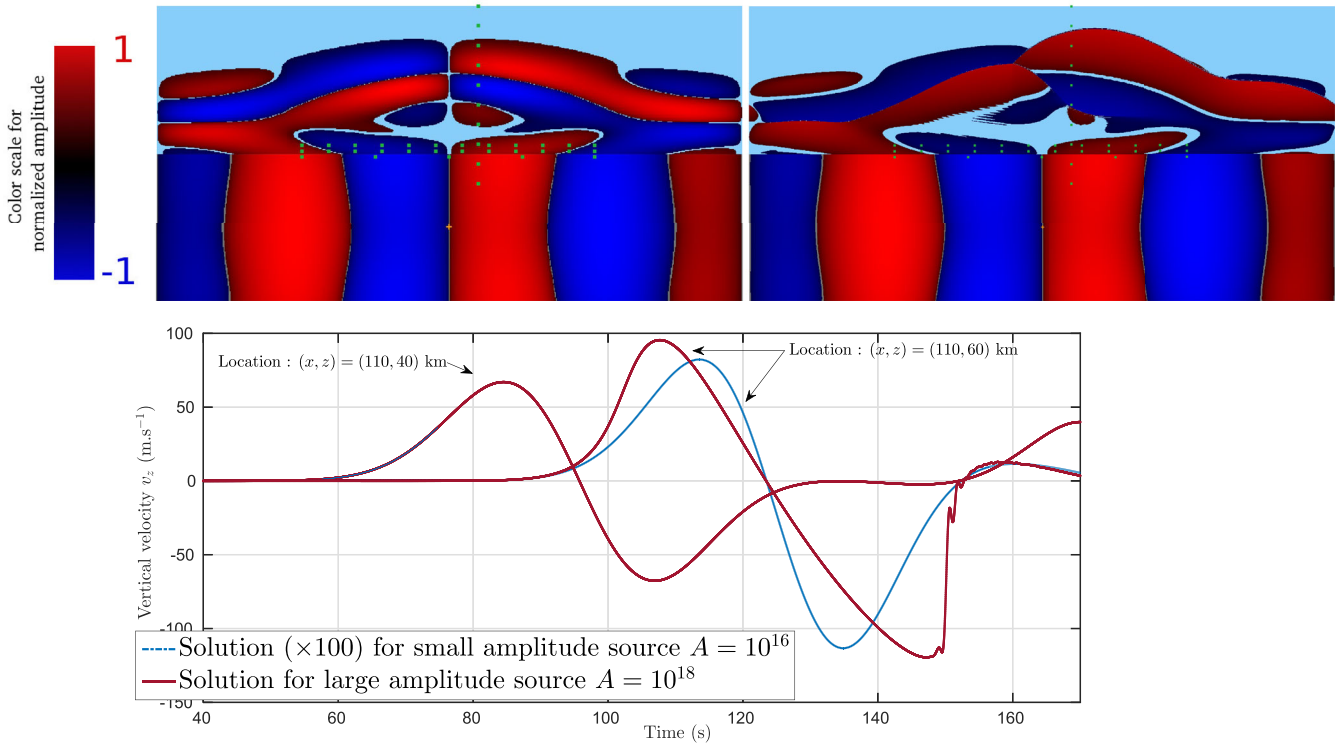

Figure 11. On the top, snapshots of vertical velocity (v_z) for the discontinuous Galerkin solution for Simulation 5.2, that is, the case of a strong seismic wave. Snapshots are shown at time $t = 170$ s. Left Figure show simulation run with a 'small-amplitude' source $A = 10^{16}$ N m and right figure simulation run with a 'large-amplitude' source $A = 10^{18}$ N m. Fluid and solid vertical velocities are normalized separately. Red colours indicate positive vertical velocities and blue colours negative ones. The green squares show the location of the recording stations. The yellow square is the source location. On the bottom, vertical velocity for the discontinuous Galerkin solution for the small amplitude source ('Solution ($\times 100$) for small amplitude source') and the large amplitude source ('Solution for large amplitude source') at different altitudes. The signals are shown through time for Simulation 5.2, that is, the case of a strong seismic wave. The comparison is shown at two recording stations located in the fluid at $(x, z) = (110, 40)$ km and at $(x, z) = (110, 60)$ km. The atmosphere is considered isothermal (Table 9).

Table 10. Simulation parameters corresponding to Model 1 from Section 4.1.1 for Simulation 5.3, that is, the case of a nonlinear gravity waves.

$L_x \times L_z$ (km)	Δx (m)	Δt (s)	ρ (kg m^{-3})	c (m s^{-1})	μ (kg m^{-1} s^{-1})	κ (W K^{-1} m^{-1})	g_z (m s^{-2})	$v_{F,x}$ (m s^{-1})
600 × 190	1500	0.1	varying	340	Varying	0	9.81	Varying

with A m s^{-1} the forcing amplitude, $\omega = 1.16 \times 10^{-3}$ rad Hz the source frequency and $c = 150$ m s^{-1} the horizontal phase speed. We select the forcing period $\tau = \frac{2\pi}{\omega} = 5417$ s. And for the exponential 'envelope' we set $F = \sqrt{\frac{8}{(\tilde{t}_0 - t_0)^2}}$ Hz with $\tilde{t}_0 = 10$ s and $t_0 = 35$ s.

The value of the amplitude forcing a will impact the long-term stability of the initial atmospheric background that will, for large values, generate convective instabilities. To observe these effects we perform two simulations with various values of amplitude $A = 10^{-3}, 10^{-1}$ m s^{-1}. We use the realistic atmosphere model from Section 4.1.2 summarized in Table 10.

Fig. 12 show the results for simulations with small (on the left) and large (on the right) forcing amplitude. Until $t = 1.8$ h simulations are similar and show the typical feature of surfaces of constant phase inclined to the horizontal at angles $\alpha \approx \arcsin \frac{\sigma}{N} \approx 18^\circ$, where N is the Brunt-Väisälä frequency ($N^2 = 3.3 \times 10^{-4}$ rad^2 s^{-2}). Beyond $t = 1.8$ h Kelvin–Helmotz instabilities start to develop, due to the movement of warmer parcels over colder parcels, which leads to the generation of a small-scale convection layer.

In Fig. 13, one notes that signals for the small forcing and large forcing are similar, but as the wave propagates and the amplitude increases wave-breaking occurs and convective instabilities develop.

6 CONCLUSIONS AND FUTURE WORK

We have considered the Navier–Stokes system of equations for acoustic and gravity wave propagation. We have implemented a coupled discontinuous and continuous Galerkin numerical scheme that handles both acoustic and gravity waves simultaneously, in 2-D. We have also taken into account nonlinearities such as acoustic shocks or gravity wave-breaking and topography.

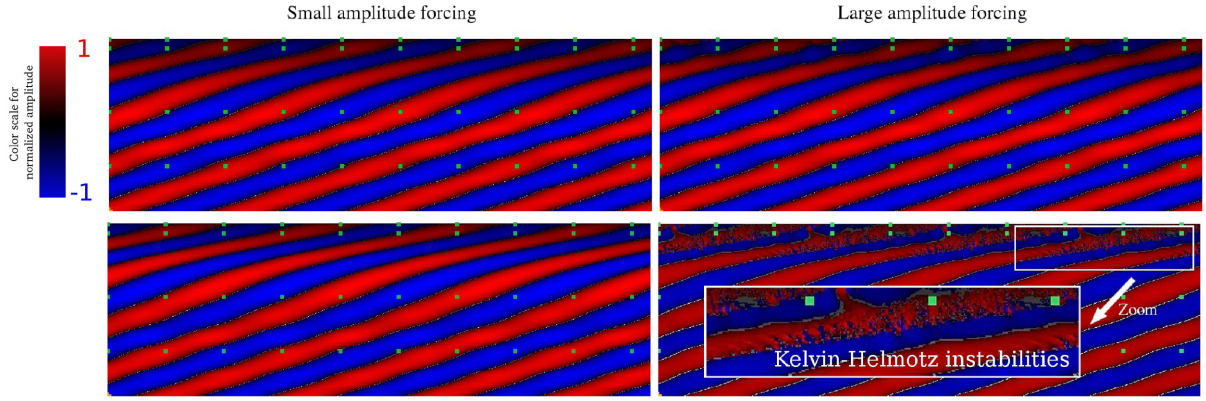

Figure 12. Snapshots of density-scaled vertical velocity ($\sqrt{\rho}v_{F,z}$) for the discontinuous Galerkin solution for Simulation 5.3, that is, the case of nonlinear gravity waves. Snapshots are shown, from top to bottom, at time $t = 1.7, 2.2$ h. Left figures show simulations with a small forcing amplitude $A = 10^{-3}$ (m s^{-1}) and right figures show simulations with strong forcing amplitude $A = 10^{-1}$ (m s^{-1}). Red indicates positive vertical velocity and blue negative ones. The green squares show the location of the recording stations. The atmosphere is considered isothermal (Table 10).

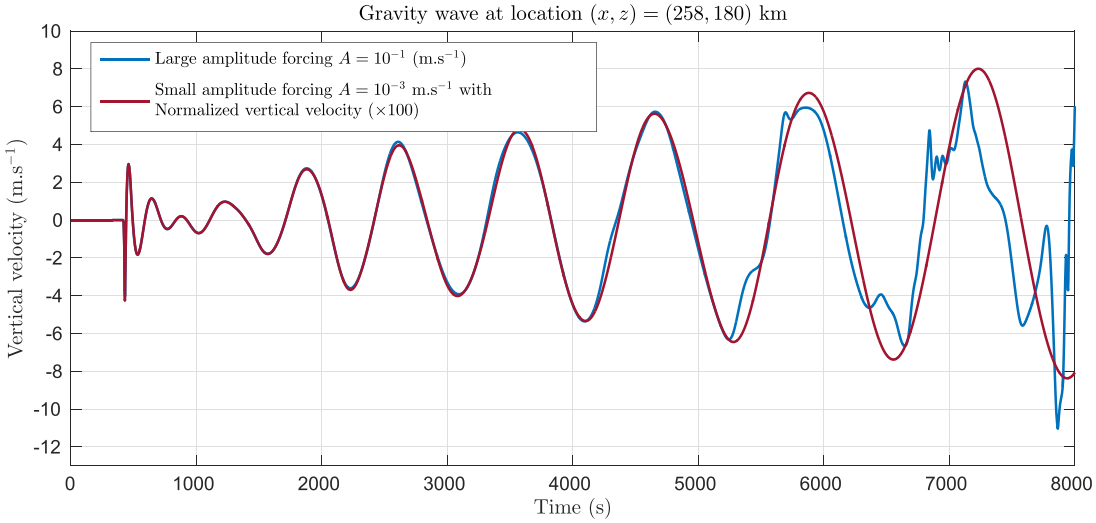

Figure 13. Vertical velocity for the discontinuous Galerkin solution for the small amplitude forcing $A = 10^{-3}$ (m s^{-1}) ('Small amplitude forcing') and the large amplitude forcing $A = 10^{-1}$ (m s^{-1}) ('Large amplitude forcing'). The small forcing signal amplitude is multiplied by 100 in order to compare it with the large amplitude forcing signal. The signals are shown through time for Simulation 5.3, that is, the case of a nonlinear gravity waves. The comparison is shown at the same recording station located at $(x, z) = (258, 180)$ km. The atmosphere is considered isothermal (Table 10).

We have validated the simulations by comparison to numerical finite-difference solutions obtained from previously published numerical technique suitable for the linear case in several benchmark cases involving acoustic and gravity waves in a stratified windy and viscous atmosphere and *P* and *S* waves in a homogeneous elastic medium. We obtained very good agreement in terms of vertical velocity and pressure. The simulation results for validation cases exhibit interesting gravity wave characteristics and show the expected features: the wave amplitude increases in vertical displacement with corresponding decrease of atmospheric density with altitude, viscosity damps high-frequency waves and strong low-frequency seismic events generate gravity waves.

We also presented nonlinear results for strong acoustic waves that convert into *N* waves as the amplitude gets large. This seems to show that waves can break for low Mach number, which needs to be studied and confirmed for more realistic media in future work. We also tackled strongly heterogeneous media with initial conditions and physical parameters based on the bulk viscosity profile from the *MSISE*-00 atmosphere model and HWM93 wind model. This showed that simulations are stable for complex media and exhibit interesting physical features such as wave breaking at high altitude for strong ground displacements due to Kelvin–Helmotz instabilities. This new numerical modelling tool can thus give insights on gravity and acoustic wave linear and nonlinear dynamics in the atmosphere due to seismic sources and/or atmospheric explosion sources.

Future developments should include more realistic non isothermal atmosphere models, absorbing boundary conditions instead of non-realistic rigid or horizontal periodic conditions in order to properly model wave propagation in the upper atmosphere. The technique should

also be extended to 3-D media and from regional to global Earth scale in order to fully understand gravity wave dynamics in planetary atmosphere.

ACKNOWLEDGEMENTS

We thank Vadim Monteiller for helpful discussions on the implementation of the discontinuous Galerkin method. Computer resources were provided by projects # p1404 at CALMIP computing centre (Toulouse, France). This work was also granted access to the French HPC resources of TGCC under allocation 2016-gen7646 made by GENCI. The authors also thank the 'Région Midi-Pyrénées' (France) and 'Université de Toulouse' for funding the PhD grant of Quentin Brissaud.

REFERENCES

Ahmad, N. & Lindeman, J., 2007. Euler solutions using flux-based wave decomposition, *Int. J. Numer. Methods Fluids,* **54**(1), 47–72.

Aki, K. & Richards, P., 1980. *Quantitative Seismology,* vol. II, Freeman & Co.

Bass, H.E. & Chambers, J.P., 2001. Absorption of sound in the Martian atmosphere, *J. acoust. Soc. Am.,* **109,** 3069–3071.

Bass, H., Sutherland, L., Piercy, J. & Evans, L., 1984. Absorption of sound by the atmosphere, in *Physical Acoustics: Principles and Methods,* vol. 17, pp. 145–232, eds Mason, W.P. & Thurston, R.N., Academic Press.

Bassi, F. & Rebay, S., 1997. A high-order accurate discontinuous finite element method for the numerical solution of the compressible Navier–Stokes equations, *J. Comput. Phys.,* **131**(2), 267–279.

Brissaud, Q., Martin, R., Garcia, R.F. & Komatitsch, D., 2016. Finite-difference numerical modelling of gravitoacoustic wave propagation in a windy and attenuating atmosphere, *Geophys. J. Int.,* **206**(1), 308–327.

Chaljub, E., Komatitsch, D., Vilotte, J.-P., Capdeville, Y., Valette, B. & Festa, G., 2007. Spectral-element analysis in seismology, *Adv. Geophys.,* **48,** 365–419.

Chandrashekar, P. & Zenk, M., 2017. Well-balanced nodal discontinuous Galerkin method for Euler equations with gravity, *J. Sci. Comp.,* **71**(3), 1062–1093.

Chidyagwai, P. & Rivière, B., 2010. Numerical modelling of coupled surface and subsurface flow systems, *Adv. Water Resour.,* **33**(1), 92–105.

Cockburn, B. & Shu, C.-W., 2001. Runge–Kutta discontinuous Galerkin methods for convection-dominated problems, *J. Sci. Comput.,* **16**(3), 173–261.

Dawson, C., 2008. A continuous/discontinuous Galerkin framework for modeling coupled subsurface and surface water flow, *Comput. Geosci.,* **12**(4), 451–472.

de Groot-Hedlin, C.D., 2016. Long-range propagation of nonlinear infrasound waves through an absorbing atmosphere, *J. acoust. Soc. Am.,* **139**(4), 1565–1577.

Dörnbrack, A. & Nappo, C.J., 1997. A note on the application of linear wave theory at a critical level, *Bound.-Layer Meteorol.,* **82**(3), 399–416.

Garcia, R.F., Bruinsma, S., Lognonné, P., Doornbos, E. & Cachoux, F., 2013. GOCE: the first seismometer in orbit around the Earth, *Geophys. Res. Lett.,* **40,** 1015–1020.

Giraldo, F.X., 1995. A space marching adaptive remeshing technique applied to the 3D Euler equations for supersonic flow, *PhD thesis,* University of Virginia, USA.

Giraldo, F.X. & Restelli, M., 2008. A study of spectral-element and discontinuous Galerkin methods for the navier–stokes equations in nonhydrostatic mesoscale atmospheric modeling: equation sets and test cases, *J. Comput. Phys.,* **227**(8), 3849–3877.

Hedin, A., 1991. Extension of the MSIS thermosphere model into the middle and lower atmosphere, *J. geophys. Res.,* **96,** 1159–1171.

Hesthaven, J.S. & Warburton, T., 2007. *Nodal Discontinuous Galerkin Methods: Algorithms, Analysis, and Applications,* Springer Science & Business Media.

Hüppe, A., Cohen, G., Imperiale, S. & Kaltenbacher, M., 2016. Construction and analysis of an adapted spectral finite element method to convective acoustic equations, *Commun. Comput. Phys.,* **20**(1), 1–22.

Käser, M. & Dumbser, M., 2008. A highly accurate discontinuous Galerkin method for complex interfaces between solids and moving fluids, *Geophysics,* **73**(3), T23–T35.

Komatitsch, D. & Tromp, J., 1999. Introduction to the spectral-element method for three-dimensional seismic wave propagation, *Geophys. J. Int.,* **139**(3), 806–822.

Komatitsch, D. & Tromp, J., 2003. A perfectly matched layer absorbing boundary condition for the second-order seismic wave equation, *Geophys. J. Int.,* **154**(1), 146–153.

Komatitsch, D., Barnes, C. & Tromp, J., 2000. Wave propagation near a fluid-solid interface: a spectral-element approach, *Geophysics,* **65**(2), 623–631.

Kopriva, D.A., 2006. Metric identities and the discontinuous spectral-element method on curvilinear meshes, *J. Sci. Comput.,* **26**(3), 301–327.

Kopriva, D.A., Woodruff, S.L. & Hussaini, M.Y., 2002. Computation of electromagnetic scattering with a non-conforming discontinuous spectral-element method, *Int. J. Numer. Methods Eng.,* **53**(1), 105–122.

Kshevetskii, S.P. & Gavrilov, N.M., 2005. Vertical propagation, breaking and effects of nonlinear gravity waves in the atmosphere, *J. Atmos. Sol.-Terr. Phys.,* **67**(11), 1014–1030.

Kursungecmez, H., 2015. Numerical simulation of shock propagation in one and two dimensional domains, *PhD thesis,* University of Edinburgh.

Landet, T., Mortensen, M. & Grue, J., 2015. Towards a continuous and discontinuous Galerkin method for multi-phase flows, in *MekIT'15 8th National Conference on Computational Mechanics,* International Center for Numerical Methods in Engineering (CIMNE), Barcelona, Spain, pp. 275–294.

Lecoanet, D., Le Bars, M., Burns, K.J., Vasil, G.M., Brown, B.P., Quataert, E. & Oishi, J.S., 2015. Numerical simulations of internal wave generation by convection in water, *Phys. Rev. E,* **91,** doi:10.1103/PhysRevE.91.063016.

LeVeque, R.J., 2002. *Finite Volume Methods for Hyperbolic Problems,* vol. 31, Cambridge Univ. Press.

Linstrom, P.J. & Mallard, W.G. (eds), 2015. *NIST Chemistry WebBook,* NIST Standard Reference Database Number 69, National Institute of Standards and Technology, Gaithersburg, MD (doi:10.18434/T4D303).

Lognonné, P., Clévédé, E. & Kanamori, H., 1998. Computation of seismograms and atmospheric oscillations by normal-mode summation for a spherical earth model with realistic atmosphere, *Geophys. J. Int.,* **135**(2), 388–406.

Mikhailenko, B. & Mikhailov, A., 2014. Numerical modeling of seismic and acoustic-gravity waves propagation in an 'earth-atmosphere' model in the presence of wind in the air, *Numer. Anal. Appl.,* **7**(2), 124–135.

Miyoshi, Y., Fujiwara, H., Jin, H. & Shinagawa, H., 2014. A global view of gravity waves in the thermosphere simulated by a general circulation model, *J. geophys. Res.,* **119**(7), 5807–5820.

Müller, A., Behrens, J., Giraldo, F.X. & Wirth, V., 2010. An adaptive discontinuous Galerkin method for modeling cumulus clouds, in *Fifth European Conference on Computational Fluid Dynamics, ECCOMAS CFD 2010,* Lisbon, Portugal.

Nappo, C., 2002. *An Introduction to Atmospheric Gravity Waves,* Academic Press.

Picone, J.M., Hedin, A.E., Drob, D.P. & Aikin, A.C., 2002. NRLMSISE-00 empirical model of the atmosphere: statistical comparisons and scientific

issues, *J. geophys. Res.,* **107**(A12), 1468, doi:10.1029/2002JA009430.
Remacle, J.-F., Flaherty, J.E. & Shephard, M.S., 2003. An adaptive discontinuous Galerkin technique with an orthogonal basis applied to compressible flow problems, *SIAM Rev.,* **45**(1), 53–72.
Schäfer, M. & Teschauer, I., 2001. Numerical simulation of coupled fluid–solid problems, *Comput. Methods Appl. Mech. Eng.,* **190**(28), 3645–3667.
Shamarock, W. *et al.*, 2008. *A Description of the Advanced Research WRF Version 3: NCAR Technical Note,* National Center for Atmospheric Research.
Shu, C.-W., 1987. TVB uniformly high-order schemes for conservation laws, *Math. Comput.,* **49**(179), 105–121.
Snively, J.B. & Pasko, V.P., 2008. Excitation of ducted gravity waves in the lower thermosphere by tropospheric sources, *J. geophys. Res.,* **113,** A06303, doi:10.1029/2007JA012693
Sod, G.A., 1978. A survey of several finite difference methods for systems of nonlinear hyperbolic conservation laws, *J. Comput. Phys.,* **27**(1), 1–31.
Spiteri, R.J. & Ruuth, S.J., 2002. A new class of optimal high-order strong-stability-preserving time discretization methods, *SIAM J. Numer. Anal.,* **40**(2), 469–491.
Tang, H. & Warnecke, G., 2005. A Runge–Kutta discontinuous Galerkin method for the Euler equations, *Comput. Fluids,* **34**(3), 375–398.
van Vossen, R., Robertsson, J.O.A. & Chapman, C.H., 2002. Finite-difference modeling of wave propagation in a fluid-solid configuration, *Geophysics,* **67**(2), 618–624.
Wei, C., Bühler, O. & Tabak, E.G., 2015. Evolution of tsunami-induced internal acoustic–gravity waves, *J. Atmos. Sci.,* **72**(6), 2303–2317.
Whitham, G.B., 2011. *Linear and Nonlinear Waves,* vol. 42, Wiley.
Ye, R., Maarten, V., Petrovitch, C.L., Pyrak-Nolte, L.J. & Wilcox, L.C., 2016. A discontinuous Galerkin method with a modified penalty flux for the propagation and scattering of acousto-elastic waves, *Geophys. J. Int.,* **205**(2), 1267–1289.
Yiğit, E. & Medvedev, A.S., 2015. Internal wave coupling processes in Earth's atmosphere, *Adv. Space Res.,* **55**(4), 983–1003.
Zuckerwar, A.J. & Ash, R.L., 2006. Variational approach to the volume viscosity of fluids, *Phys. Fluids,* **18,**, 047101, doi:10.1063/1.2180780.

APPENDIX A: RAYLEIGH–TAYLOR INSTABILITY

The Rayleigh–Taylor problem involves a heavy (cold) fluid overlying a light (warm) fluid. We consider two inviscid fluids initially in a cavity where upper half of the cavity is a fluid of density 2 while the lower part is a fluid of unit density. The initial pressure corresponds to hydrostatic equilibrium described in Section 2.5. Initial density and pressure profiles read

$$p = \begin{cases} p_0 e^{-\frac{z-z_0}{RT_l}} & \text{if } z > 0.5 \\ p_0 e^{-\frac{z-z_0}{RT_h}} & \text{if } z \leq 0.5 \end{cases}$$

$$\rho = \begin{cases} \frac{p}{RT_l} & \text{if } z > 0.5 \\ \frac{p}{RT_h} & \text{if } z \leq 0.5 \end{cases} \tag{A1}$$

where $R = C_p - C_v = 1$ (kg m^2 s^{-2} K^{-1}) and $T_h = 2$ °C (respectively $T_l = 1$ °C) are temperature of the top heavy fluid (respectively lower light fluid). Other unknowns are described in Table A1.

Fig. A1 shows the physically unstable initial condition configuration where instabilities eventually grow as the heavy fluid penetrates the lighter one due to gravity. No shocks occur in this compressible problem and the only discontinuity is the contact surface separating the fluids of different densities. As pointed out in Remacle *et al.* (2003) the limiting procedure tends to strongly diffuse the interface but as we do not consider strong interface discontinuities in our applications, the numerical method works efficiently enough.

Table A1. Simulation parameters corresponding to Simulation A, that is, the case of a Rayleigh–Taylor instability.

$L_x \times L_z$ (km)	Δx (m)	Δt (s)	ρ (kg m^{-3})	c (m s^{-1})	μ (kg m^{-1} s^{-1})	κ (W K^{-1} m^{-1})	g_z (m s^{-2})	$v_{F,x}$ (m s^{-1})
0.25 × 1	0.01	10^{-3}	Varying	340	0	0	−1	0

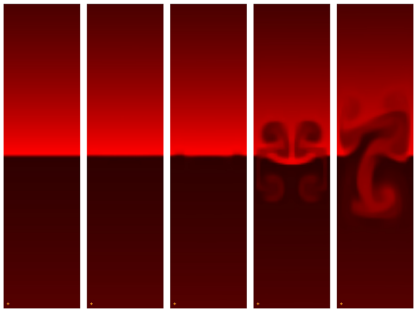

Figure A1. From left to right, snapshots of density at times $t = 0.005$, 2.5, 5, 7.5, 10 s, respectively, for Simulation A, that is, the case of a Rayleigh–Taylor instability. Density values are normalized using the largest density value in the mesh independently at each time step. The darkest red shades represent the smallest density values and, conversely, lightest red shades represent for the largest values. Until $t = 5$ s the boundary remains stable, and then instabilities develop.

APPENDIX B: RISING THERMAL BUBBLE

This classical test case (Giraldo & Restelli 2008) corresponds to the evolution of a warm bubble in constant potential temperature fluid. The bubble will rise in the fluid, since it is warmer than the ambient fluid, and deform due to shearing motion and form mushroom clouds. The initial density and pressure profiles are

$$\begin{aligned}
\theta &= \begin{cases} 300 & \text{if } r > 0.1 \\ 150.25(1+\cos\frac{\pi r}{0.1}) & \text{if } r \le 0.1 \end{cases} \\
\tilde{\pi} &= \frac{-gz}{C_p\theta} + 10^{-2} \\
p &= p_0\tilde{\pi}^{\frac{C_p}{R}} \\
\rho &= \frac{p_0}{R\theta}\tilde{\pi}^{\frac{C_v}{R}}
\end{aligned} \quad , \tag{B1}$$

where $r = \sqrt{(x-x_0)^2 + (z-z_0)^2}$ is the bubble radius with $x_0 = 0.5$ m and $z_0 = 0.35$ m, $R = C_p - C_v = 2$, $\tilde{\pi} = (\frac{p}{p_0})^{\frac{R}{C_p}}$ is the Exner pressure, and $\theta = \frac{T}{\tilde{\pi}}$ is the potential temperature. The simulation setup is given by eq. (B1) and summarized in Table B1.

As described earlier, in the initial neutral atmosphere the smooth potential temperature perturbation generates vertical upward and shear velocities that makes the bubble rising and, through time, deforming, and transitioning to turbulence. This test shows ability to capture the effects of turbulence and turbulent convection. Although no analytical solution is available, the numerical results are physically plausible and are qualitatively similar to the 2-D experiment in Giraldo & Restelli (2008).

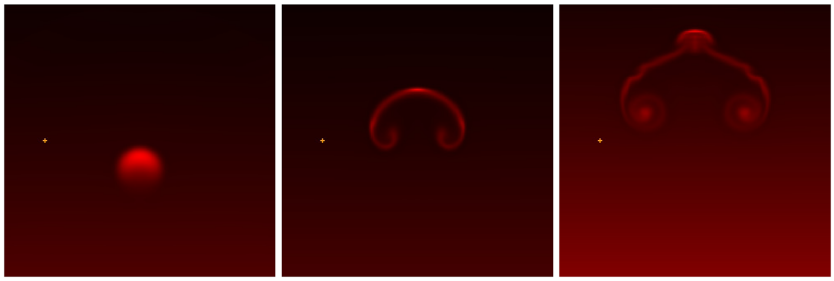

Figure B1. From left to right, snapshots of density at times $t = 0.24$, 0.75, 1.2 s respectively for Simulation B, that is, the case of a rising thermal bubble. Density values are normalized using the largest density value in the mesh at each time step. The darkest red shades are for the smallest density values and the lightest are for the largest values.

Table B1. Simulation parameters corresponding to Simulation B, that is, the case of a rising thermal bubble.

$L_x \times L_z$ (m)	Δx (m)	Δt (s)	ρ (kg m^{-3})	c (m s^{-1})	μ (kg m^{-1} s^{-1})	κ (W K^{-1} m^{-1})	g_z (m s^{-2})	$v_{F,x}$ (m s^{-1})
1×1	0.01	10^{-4}	Varying	Varying	0	0	9.81	0